

Fractals and Wavelets

1 *What Can We Learn on Transcription 2 and Replication from Wavelet-Based 3 Multifractal Analysis of DNA Sequences?*

4 ALAIN ARNEODO¹, BENJAMIN AUDIT¹,
5 EDWARD-BENEDICT BRODIE OF BRODIE¹,
6 SAMUEL NICOLAY², MARIE TOUCHON^{3,5},
7 YVES D'AUBENTON-CARAFA⁴, MAXIME HUVET⁴,
8 CLAUDE THERMES⁴

9 ¹ Laboratoire Joliot-Curie and Laboratoire de Physique,
10 ENS-Lyon CNRS, Lyon Cedex, France

11 ² Institut de Mathématique, Université de Liège,
12 Liège, Belgium

13 ³ Génétique des Génomes Bactériens, Institut Pasteur,
14 CNRS, Paris, France

15 ⁴ Centre de Génétique Moléculaire, CNRS,
16 Gif-sur-Yvette, France

17 ⁵ Atelier de Bioinformatique, Université Pierre
18 et Marie Curie, Paris, France

19 Article Outline

- 20 Glossary
- 21 Definition of the Subject
- 22 Introduction
- 23 A Wavelet-Based Multifractal Formalism:
 - 24 The Wavelet Transform Modulus Maxima Method
 - 25 Bifractality of Human DNA Strand-Asymmetry Profiles
 - 26 Results from Transcription
 - 27 From the Detection of Relocation Origins Using
 - 28 the Wavelet Transform Microscope to the Modeling
 - 29 of Replication in Mammalian Genomes
 - 30 A Wavelet-Based Methodology to Disentangle
 - 31 Transcription- and Replication-Associated Strand
 - 32 Asymmetries Reveals a Remarkable Gene Organization
 - 33 in the Human Genome
 - 34 Future Directions
 - 35 Acknowledgments
 - 36 Bibliography

37 Glossary

- 38 **Fractal** Fractals are complex mathematical objects that
- 39 are invariant with respect to dilations (**self-similarity**)
- 40 and therefore do not possess a characteristic length
- 41 scale. Fractal objects display scale-invariance proper-
- 42 ties that can either fluctuate from point to point (**mul-**
- 43 **tifractal**) or be homogeneous (**monofractal**). Mathe-
- 44 matically, these properties should hold over all scales.

However, in the real world, there are necessarily lower
and upper bounds over which self-similarity applies.

Wavelet transform The continuous wavelet transform
(WT) is a mathematical technique introduced in the
early 1980s to perform time-frequency analysis. The
WT has been early recognized as a mathematical mi-
croscope that is well adapted to characterize the scale-
invariance properties of fractal objects and to reveal
the hierarchy that governs the spatial distribution of
the singularities of multifractal measures and func-
tions. More specifically, the WT is a space-scale anal-
ysis which consists in expanding signals in terms of
wavelets that are constructed from a single function,
the analyzing wavelet, by means of translations and di-
lations.

59 Wavelet transform modulus maxima method

The WTMM method provides a unified statistical
(thermodynamic) description of multifractal distribu-
tions including measures and functions. This method
relies on the computation of partition functions from
the wavelet transform skeleton defined by the wavelet
transform modulus maxima (WTMM). This skeleton
provides an adaptive space-scale partition of the frac-
tal distribution under study, from which one can ex-
tract the $D(h)$ singularity spectrum as the equivalent
of a thermodynamic potential (entropy). With some
appropriate choice of the analyzing wavelet, one can
show that the WTMM method provides a natural gen-
eralization of the classical box-counting and structure
function techniques.

Compositional strand asymmetry The DNA double hel-
ix is made of two strands that are maintained to-
gether by hydrogen bonds involved in the base-pair-
ing between Adenine (resp. Guanine) on one strand
and Thymine (resp. Cytosine) on the other strand.
Under no-strand bias conditions, i. e. when mutation
rates are identical on the two strands, in other words
when the two strands are strictly equivalent, one ex-
pects equimolarities of adenine and thymine and of
guanine and cytosine on each DNA strand, a property
named Chargaff's second parity rule. Compositional
strand asymmetry refers to deviations from this rule
which can be assessed by measuring departure from
intrastrand equimolarities. Note that two major bio-
logical processes, **transcription** and **replication**, both
requiring the opening of the double helix, actually
break the symmetry between the two DNA strands and
can thus be at the origin of compositional strand asym-
metries.

Eukaryote Organisms whose cells contain a nucleus, the
structure containing the genetic material arranged into

Please note that the pagination is not final; in the print version an entry will in general not start on a new page.

96 chromosomes. Eukaryotes constitute one of the three
 97 domains of life, the two others, called prokaryotes
 98 (without nucleus), being the eubacteria and the ar-
 99 chaebacteria.

100 **Transcription** Transcription is the process whereby the
 101 DNA sequence of a gene is enzymatically copied into
 102 a complementary messenger RNA. In a following step,
 103 **translation** takes place where each messenger RNA
 104 serves as a template to the biosynthesis of a specific
 105 protein.

106 **Replication** DNA replication is the process of making an
 107 identical copy of a double-stranded DNA molecule.
 108 DNA replication is an essential cellular function re-
 109 sponsible for the accurate transmission of genetic in-
 110 formation though successive cell generations. This
 111 process starts with the binding of initiating proteins to
 112 a DNA locus called **origin of replication**. The recruit-
 113 ment of additional factors initiates the bi-directional
 114 progression of two replication forks along the chromo-
 115 some. In eukaryotic cells, this binding event happens
 116 at a multitude of replication origins along each chro-
 117 mosome from which replication propagates until two
 118 converging forks collide at a **terminus of replication**.

119 **Chromatin** Chromatin is the compound of DNA and
 120 proteins that forms the chromosomes in living cells. In
 121 eukaryotic cells, chromatin is located in the nucleus.

122 **Histones** Histones are a major family of proteins found in
 123 eukaryotic chromatin. The wrapping of DNA around
 124 a core of 8 histones forms a **nucleosome**, the first step
 125 of eukaryotic DNA compaction.

144 in the choice of these “generalized oscillating boxes” to get
 145 rid of possible (smooth) polynomial behavior that might
 146 either mask singularities or perturb the estimation of their
 147 strength h (Hölder exponent), remedying in this way for
 148 one of the main failures of the classical multifractal meth-
 149 ods (e.g. the box-counting algorithms in the case of mea-
 150 sures and the structure function method in the case of
 151 functions [12,13,15,16]). The other fundamental advan-
 152 tage of using wavelets is that the skeleton defined by the
 153 WTMM [10,11], provides an adaptative space-scale parti-
 154 tioning from which one can extract the $D(h)$ singularity
 155 spectrum via the Legendre transform of the scaling expo-
 156 nents $\tau(q)$ (q real, positive as well as negative) of some par-
 157 tition functions defined from the WT skeleton. We refer
 158 the reader to Bacry et al. [13], Jaffard [17,18] for rigorous
 159 mathematical results and to Hentschel [19] for the theo-
 160 retical treatment of random multifractal functions.

161 Applications of the WTMM method to 1D signals
 162 have already provided insights into a wide variety of prob-
 163 lems [20], e.g., the validation of the log-normal cascade
 164 phenomenology of fully developed turbulence [21,22,23,
 165 24] and of high-resolution temporal rainfall [25,26], the
 166 characterization and the understanding of long-range cor-
 167 relations in DNA sequences [27,28,29,30], the demonstra-
 168 tion of the existence of causal cascade of information from
 169 large to small scales in financial time series [31,32], the
 170 use of the multifractal formalism to discriminate between
 171 healthy and sick heartbeat dynamics [33,34], the discov-
 172 ery of a Fibonacci structural ordering in 1D cuts of diffu-
 173 sion limited aggregates (DLA) [35,36,37,38]. The canon-
 174 ical WTMM method has been further generalized from 1D
 175 to 2D with the specific goal to achieve multifractal analy-
 176 sis of rough surfaces with fractal dimensions D_F anywhere
 177 between 2 and 3 [39,40,41]. The 2D WTMM method has
 178 been successfully applied to characterize the intermittent
 179 nature of satellite images of the cloud structure [42,43], to
 180 perform a morphological analysis of the anisotropic struc-
 181 ture of atomic hydrogen (H_I) density in Galactic spiral
 182 arms [44] and to assist in the diagnosis in digitized mam-
 183 mograms [45]. We refer the reader to Arneodo et al. [46]
 184 for a review of the 2D WTMM methodology, from the the-
 185 oretical concepts to experimental applications. In a recent
 186 work, Kestener and Arneodo [47] have further extended
 187 the WTMM method to 3D analysis. After some convinc-
 188 ing test applications to synthetic 3D monofractal Brown-
 189 ian fields and to 3D multifractal realizations of singular
 190 cascade measures as well as their random function coun-
 191 terpart obtained by fractional integration, the 3D WTMM
 192 method has been applied to dissipation and enstrophy 3D
 193 numerical data issued from direct numerical simulations
 194 (DNS) of isotropic turbulence. The results so-obtained

126 **Definition of the Subject**

127 The continuous wavelet transform (WT) is a mathemat-
 128 ical technique introduced in signal analysis in the early
 129 1980s [1,2]. Since then, it has been the subject of consid-
 130 erable theoretical developments and practical applications
 131 in a wide variety of fields. The WT has been early recog-
 132 nized as a mathematical microscope that is well adapted
 133 to reveal the hierarchy that governs the spatial distribu-
 134 tion of singularities of multifractal measures [3,4,5]. What
 135 makes the WT of fundamental use in the present study
 136 is that its singularity scanning ability equally applies to
 137 singular functions than to singular measures [3,4,5,6,7,
 138 8,9,10,11]. This has led Alain Arneodo and his collabo-
 139 rators [12,13,14,15,16] to elaborate a unified thermody-
 140 namic description of multifractal distributions including
 141 measures and functions, the so-called Wavelet Transform
 142 Modulus Maxima (WTMM) method. By using wavelets
 143 instead of boxes, one can take advantage of the freedom

195 have revealed that the multifractal spatial structure of both
 196 dissipation and enstrophy fields are likely to be well de-
 197 scribed by a multiplicative cascade process clearly non-
 198 conservative. This contrasts with the conclusions of previ-
 199 ous box-counting analysis [48] that failed to estimate cor-
 200 rectly the corresponding multifractal spectra because of
 201 their intrinsic inability to master non-conservative singu-
 202 lar cascade measures [47].

203 For many years, the multifractal description has been
 204 mainly devoted to scalar measures and functions. How-
 205 ever, in physics as well as in other fundamental and ap-
 206 plied sciences, fractals appear not only as deterministic or
 207 random scalar fields but also as vector-valued determin-
 208 istic or random fields. Very recently, Kestener and Ar-
 209 neodo [49,50] have combined singular value decomposi-
 210 tion techniques and WT analysis to generalize the mul-
 211 trifractal formalism to vector-valued random fields. The
 212 so-called Tensorial Wavelet Transform Modulus Maxima
 213 (TWTMM) method has been applied to turbulent velocity
 214 and vorticity fields generated in (256)³ DNS of the incom-
 215 pressible Navier–Stokes equations. This study reveals the
 216 existence of an intimate relationship $D_v(h+1) = D_\omega(h)$
 217 between the singularity spectra of these two vector fields
 218 that are found significantly more intermittent than previ-
 219 ously estimated from longitudinal and transverse veloc-
 220 ity increment statistics. Furthermore, thanks to the singu-
 221 lar value decomposition, the TWTMM method looks very
 222 promising for future simultaneous multifractal and struc-
 223 tural (vorticity sheets, vorticity filaments) analysis of tur-
 224 bulent flows [49,50].

225 Introduction

226 The possible relevance of scale invariance and fractal con-
 227 cepts to the structural complexity of genomic sequences
 228 has been the subject of considerable increasing inter-
 229 est [20,51,52]. During the past fifteen years or so, there
 230 has been intense discussion about the existence, the na-
 231 ture and the origin of the long-range correlations (LRC)
 232 observed in DNA sequences. Different techniques includ-
 233 ing mutual information functions [53,54], auto-correla-
 234 tion functions [55,56], power-spectra [54,57,58], “DNA
 235 walk” representation [52,59], Zipf analysis [60,61] and en-
 236 tropies [62,63], were used for the statistical analysis of
 237 DNA sequences. For years there has been some perma-
 238 nent debate on rather struggling questions like the fact that
 239 the reported LRC might be just an artifact of the composi-
 240 tional heterogeneity of the genome organization [20,27,52,
 241 55,56,64,65,66,67]. Another controversial issue is whether
 242 or not LRC properties are different for protein-coding (ex-
 243 onic) and non-coding (intronic, intergenic) sequences [20,

244 27,52,54,55,56,57,58,59,61,68]. Actually, there were many
 245 objective reasons for this somehow controversial situation.
 246 Most of the pioneering investigations of LRC in DNA se-
 247 quences were performed using different techniques that
 248 all consisted in measuring power-law behavior of some
 249 characteristic quantity, e. g., the fractal dimension of the
 250 DNA walk, the scaling exponent of the correlation func-
 251 tion or the power-law exponent of the power spectrum.
 252 Therefore, in practice, they all faced the same difficulties,
 253 namely finite-size effects due to the finiteness of the se-
 254 quence [69,70,71] and statistical convergence issue that
 255 required some precautions when averaging over many
 256 sequences [52,65]. But beyond these practical problems,
 257 there was also a more fundamental restriction since the
 258 measurement of a unique exponent characterizing the
 259 global scaling properties of a sequence failed to resolve
 260 multifractality [27], and thus provided very poor informa-
 261 tion upon the nature of the underlying LRC (if they were
 262 any). Actually, it can be shown that for a homogeneous
 263 (monofractal) DNA sequence, the scaling exponents esti-
 264 mated with the techniques previously mentioned, can all
 265 be expressed as a function of the so-called Hurst or rough-
 266 ness exponent H of the corresponding DNA walk land-
 267 scape [20,27,52]. $H = 1/2$ corresponds to classical Brown-
 268 ian, i. e. uncorrelated random walk. For any other value
 269 of H , the steps (increments) are either positively corre-
 270 lated ($H > 1/2$: Persistent random walk) or anti-correlated
 271 ($H < 1/2$: Anti-persistent random walk).

272 One of the main obstacles to LRC analysis in DNA
 273 sequences is the genuine mosaic structure of these se-
 274 quences which are well known to be formed of “patches”
 275 of different underlying composition [72,73,74]. When us-
 276 ing the “DNA walk” representation, these patches appear
 277 as trends in the DNA walk landscapes that are likely to
 278 break scale-invariance [20,52,59,64,65,66,67,75,76]. Most
 279 of the techniques, e. g. the variance method, used for char-
 280 acterizing the presence of LRC are not well adapted to
 281 study non-stationary sequences. There have been some
 282 phenomenological attempts to differentiate local patch-
 283 iness from LRC using ad hoc methods such as the so-
 284 called “min-max method” [59] and the “detrended fluc-
 285 tuation analysis” [77]. In previous works [27,28], the WT
 286 has been emphasized as a well suited technique to over-
 287 come this difficulty. By considering analyzing wavelets that
 288 make the WT microscope blind to low-frequency trends,
 289 any bias in the DNA walk can be removed and the ex-
 290 istence of power-law correlations with specific scale in-
 291 variance properties can be revealed accurately. In [78],
 292 from a systematic WT analysis of human exons, CDSs
 293 and introns, LRC were found in non-coding sequences as
 294 well as in coding regions somehow hidden in their inner

295 codon structure. These results made rather questionable
 296 the model based on genome plasticity proposed at that
 297 time to account for the reported absence of LRC in coding
 298 sequences [27,28,52,54,59,68]. More recently, some struc-
 299 tural interpretation of these LRC has emerged from a com-
 300 parative multifractal analysis of DNA sequences using
 301 structural coding tables based on nucleosome positioning
 302 data [29,30]. The application of the WTMM method has
 303 revealed that the corresponding DNA chain bending pro-
 304 files are monofractal (homogeneous) and that there exists
 305 two LRC regimes. In the 10–200 bp range, LRC are ob-
 306 served for eukaryotic sequences as quantified by a Hurst
 307 exponent value $H \simeq 0.6$ (but not for eubacterial sequences
 308 for which $H = 0.5$) as the signature of the nucleosomal
 309 structure. These LRC were shown to favor the autonomous
 310 formation of small (a few hundred bps) 2D DNA loops
 311 and in turn the propensity of eukaryotic DNA to inter-
 312 act with histones to form nucleosomes [79,80]. In addition,
 313 these LRC might induce some local hyperdiffusion
 314 of these loops which would be a very attractive interpre-
 315 tation of the nucleosomal repositioning dynamics. Over
 316 larger distances ($\gtrsim 200$ bp), stronger LRC with $H \simeq 0.8$
 317 seem to exist in any sequence [29,30]. These LRC are ac-
 318 tually observed in the *S. cerevisiae* nucleosome position-
 319 ing data [81] suggesting that they are involved in the nu-
 320 cleosome organization in the so-called 30 nm chromatin
 321 fiber [82]. The fact that this second regime of LRC is also
 322 present in eubacterial sequences shows that it is likely to
 323 be a possible key to the understanding of the structure and
 324 dynamics of both eukaryotic and prokaryotic chromatin
 325 fibers. In regards to their potential role in regulating the
 326 hierarchical structure and dynamics of chromatin, the re-
 327 cent report [83] of sequence-induced LRC effects on the
 328 conformations of naked DNA molecules deposited onto
 329 mica surface under 2D thermodynamic equilibrium ob-
 330 served by Atomic Force Microscopy (AFM) is a definite
 331 experimental breakthrough.

332 Our purpose here is to take advantage of the avail-
 333 ability of fully sequenced genomes to generalize the ap-
 334 plication of the WTMM method to genome-wide mul-
 335tifractal sequence analysis when using codings that have
 336 a clear functional meaning. According to the second par-
 337 ity rule [84,85], under no strand-bias conditions, each
 338 genomic DNA strand should present equimolarities of
 339 adenines A and thymines T and of guanines G and cy-
 340 tosines C [86,87]. Deviations from intrastrand equimolar-
 341 ities have been extensively studied during the past decade
 342 and the observed skews have been attributed to asym-
 343 metries intrinsic to the replication and transcription pro-
 344 cesses that both require the opening of the double helix.
 345 Actually, during these processes mutational events can af-

fect the two strands differently and an asymmetry can
 346 result if one strand undergoes different mutations, or
 347 is repaired differently than the other strand. The exis-
 348 tence of transcription and/or replication associated strand
 349 asymmetries has been mainly established for prokaryote,
 350 organelle and virus genomes [88,89,90,91,92,93,94]. For
 351 a long time the existence of compositional biases in eu-
 352 karyotic genomes has been unclear and it is only recently
 353 that (i) the statistical analysis of eukaryotic gene introns
 354 have revealed the presence of transcription-coupled strand
 355 asymmetries [95,96,97] and (ii) the genome wide multi-
 356 scale analysis of mammalian genomes has clearly shown
 357 some departure from intrastrand equimolarities in inter-
 358 genic regions and further confirmed the existence of repli-
 359 cation-associated strand asymmetries [98,99,100]. In this
 360 manuscript, we will review recent results obtained when
 361 using the WT microscope to explore the scale invariance
 362 properties of the TA and GC skew profiles in the 22 hu-
 363 man autosomes [98,99,100]. These results will enlighten
 364 the richness of information that can be extracted from
 365 these functional codings of DNA sequences including the
 366 prediction of 1012 putative human replication origins. In
 367 particular, this study will reveal a remarkable human gene
 368 organization driven by the coordination of transcription
 369 and replication [101].

A Wavelet-Based Multifractal Formalism: The Wavelet Transform Modulus Maxima Method

The Continuous Wavelet Transform

The WT is a space-scale analysis which consists in expand-
 374 ing signals in terms of *wavelets* which are constructed from
 375 a single function, the *analyzing wavelet* ψ , by means of
 376 translations and dilations. The WT of a real-valued func-
 377 tion f is defined as [1,2]:

$$T_\psi[f](x_0, a) = \frac{1}{a} \int_{-\infty}^{+\infty} f(x) \psi\left(\frac{x - x_0}{a}\right) dx, \quad (1) \quad 379$$

where x_0 is the space parameter and $a (> 0)$ the scale pa-
 380 rameter. The analyzing wavelet ψ is generally chosen to be
 381 well localized in both space and frequency. Usually ψ is re-
 382 quired to be of zero mean for the WT to be invertible. But
 383 for the particular purpose of singularity tracking that is of
 384 interest here, we will further require ψ to be orthogonal to
 385 low-order polynomials [7,8,9,10,11,12,13,14,15,16]:

$$\int_{-\infty}^{+\infty} x^m \psi(x) dx, \quad 0 \leq m < n_\psi. \quad (2) \quad 387$$

TS2 Please check. Fig. 2 is cited before Fig. 1.

388 As originally pointed out by Mallat and collabora-
 389 tors [10,11], for the specific purpose of analyzing the reg-
 390 ularity of a function, one can get rid of the redundancy of
 391 the WT by concentrating on the WT skeleton defined by
 392 its modulus maxima only. These maxima are defined, at
 393 each scale a , as the local maxima of $|T_\psi[f](x, a)|$ consid-
 394 ered as a function of x . As illustrated in Figs. 2e, 2f^{TS2},
 395 these WTMM are disposed on connected curves in the
 396 space-scale (or time-scale) half-plane, called *maxima lines*.
 397 Let us define $\mathcal{L}(a_0)$ as the set of all the maxima lines that
 398 exist at the scale a_0 and which contain maxima at any scale
 399 $a \leq a_0$. An important feature of these maxima lines, when
 400 analyzing singular functions, is that there is at least one
 401 maxima line pointing towards each singularity [10,11,16].

402 Scanning Singularities with the Wavelet 403 Transform Modulus Maxima

404 The strength of the singularity of a function f at point x_0
 405 is given by the *Hölder* exponent, i. e., the largest exponent
 406 such that there exists a polynomial $P_n(x - x_0)$ of order
 407 $n < h(x_0)$ and a constant $C > 0$, so that for any point x
 408 in a neighborhood of x_0 , one has [7,8,9,10,11,13,16]:

$$409 \quad |f(x) - P_n(x - x_0)| \leq C |x - x_0|^h. \quad (3)$$

410 If f is n times continuously differentiable at the point x_0 ,
 411 then one can use for the polynomial $P_n(x - x_0)$, the order-
 412 n Taylor series of f at x_0 and thus prove that $h(x_0) > n$.
 413 Thus $h(x_0)$ measures how irregular the function f is at the
 414 point x_0 . The higher the exponent $h(x_0)$, the more regular
 415 the function f .

416 The main interest in using the WT for analyzing the
 417 regularity of a function lies in its ability to be blind to
 418 polynomial behavior by an appropriate choice of the an-
 419 alyzing wavelet ψ . Indeed, let us assume that according
 420 to Eq. (3), f has, at the point x_0 , a local scaling (Hölder)
 421 exponent $h(x_0)$; then, assuming that the singularity is not
 422 oscillating [11,102,103], one can easily prove that the local
 423 behavior of f is mirrored by the WT which locally behaves
 424 like [7,8,9,10,11,12,13,14,15,16,17,18]:

$$425 \quad T_\psi[f](x_0, a) \sim a^{h(x_0)}, \quad a \rightarrow 0^+, \quad (4)$$

426 provided $n_\psi > h(x_0)$, where n_ψ is the number of vanish-
 427 ing moments of ψ (Eq. (2)). Therefore one can extract the
 428 exponent $h(x_0)$ as the slope of a log-log plot of the WT am-
 429 plitude versus the scale a . On the contrary, if one chooses
 430 $n_\psi < h(x_0)$, the WT still behaves as a power-law but with
 431 a scaling exponent which is n_ψ :

$$432 \quad T_\psi[f](x_0, a) \sim a^{n_\psi}, \quad a \rightarrow 0^+. \quad (5)$$

Thus, around a given point x_0 , the faster the WT decreases
 433 when the scale goes to zero, the more regular f is around
 434 that point. In particular, if $f \in C^\infty$ at x_0 ($h(x_0) = +\infty$),
 435 then the WT scaling exponent is given by n_ψ , i. e. a value
 436 which is dependent on the shape of the analyzing wavelet.
 437 According to this observation, one can hope to detect the
 438 points where f is smooth by just checking the scaling be-
 439 havior of the WT when increasing the order n_ψ of the an-
 440 alyzing wavelet [12,13,14,15,16].
 441

Remark 1 A very important point (at least for practical
 442 purpose) raised by Mallat and Hwang [10] is that the local
 443 scaling exponent $h(x_0)$ can be equally estimated by looking
 444 at the value of the WT modulus along a maxima line con-
 445 verging towards the point x_0 . Indeed one can prove that
 446 both Eqs. (4) and (5) still hold when following a maxima
 447 line from large down to small scales [10,11].
 448

449 A Wavelet-Based Multifractal Formalism: 450 The Wavelet Transform Modulus Maxima Method

As originally defined by Parisi and Frisch [104], the multi-
 451 fractal formalism of multi-affine functions amounts to
 452 compute the so-called *singularity spectrum* $D(h)$ defined
 453 as the Hausdorff dimension of the set where the Hölder
 454 exponent is equal to h [12,13,16]:
 455

$$456 \quad D(h) = \dim_H \{x, h(x) = h\}, \quad (6)$$

where h can take, a priori, positive as well as negative real
 457 values (e. g., the Dirac distribution $\delta(x)$ corresponds to the
 458 Hölder exponent $h(0) = -1$) [17].
 459

A natural way of performing a multifractal analysis
 460 of fractal functions consists in generalizing the “classi-
 461 cal” multifractal formalism [105,106,107,108,109] using
 462 wavelets instead of boxes. By taking advantage of the free-
 463 dom in the choice of the “generalized oscillating boxes”
 464 that are the wavelets, one can hope to get rid of possible
 465 smooth behavior that could mask singularities or perturb
 466 the estimation of their strength h . But the major difficulty
 467 with respect to box-counting techniques [48,106,110,111,
 468 112] for singular measures, consists in defining a covering
 469 of the support of the singular part of the function with our
 470 set of wavelets of different sizes. As emphasized in [12,13,
 471 14,15,16], the branching structure of the WT skeletons of
 472 fractal functions in the (x, a) half-plane enlightens the hi-
 473 erarchical organization of their singularities (Figs. 2e, 2f).
 474 The WT skeleton can thus be used as a guide to position,
 475 at a considered scale a , the oscillating boxes in order to
 476 obtain a partition of the singularities of f . The wavelet
 477 transform modulus maxima (WTMM) method amounts
 478 to compute the following partition function in terms of
 479

480 WTMM coefficients [12,13,14,15,16]:

481
$$Z(q, a) = \sum_{l \in \mathcal{L}(a)} \left(\sup_{\substack{(x, a') \in l \\ a' \leq a}} |T_\psi[f](x, a')| \right)^q, \quad (7)$$

482 where $q \in \mathbb{R}$ and the sup can be regarded as a way to
483 define a scale adaptative “Hausdorff-like” partition. Now
484 from the deep analogy that links the multifractal formalism
485 to thermodynamics [12,113], one can define the ex-
486 ponent $\tau(q)$ from the power-law behavior of the partition
487 function:

488
$$Z(q, a) \sim a^{\tau(q)}, \quad a \rightarrow 0^+, \quad (8)$$

489 where q and $\tau(q)$ play respectively the role of the inverse
490 temperature and the free energy. The main result of this
491 wavelet-based multifractal formalism is that in place of the
492 energy and the entropy (i. e. the variables conjugated to q
493 and τ), one has h , the Hölder exponent, and $D(h)$, the sin-
494 gularity spectrum. This means that the singularity spec-
495 trum of f can be determined from the Legendre transform
496 of the partition function scaling exponent $\tau(q)$ [13,17,18]:

497
$$D(h) = \min_q (qh - \tau(q)). \quad (9)$$

498 From the properties of the Legendre transform, it is easy to
499 see that *homogeneous* fractal functions that involve singu-
500 larities of unique Hölder exponent $h = \partial\tau/\partial q$, are char-
501 acterized by a $\tau(q)$ spectrum which is a *linear* function
502 of q . On the contrary, a *nonlinear* $\tau(q)$ curve is the signa-
503 ture of nonhomogeneous functions that exhibit *multiprac-
504 tal* properties, in the sense that the Hölder exponent $h(x)$
505 is a fluctuating quantity that depends upon the spatial po-
506 sition x .507

Defining our Battery of Analyzing Wavelets

508 There are almost as many analyzing wavelets as applica-
509 tions of the continuous WT [3,4,5,12,13,14,15,16]. In the
510 present work, we will mainly used the class of analyzing
511 wavelets defined by the successive derivatives of the Gauss-
512 ian function:

513
$$g^{(N)}(x) = \frac{dx^N}{dx^N} e^{-x^2/2}, \quad (10)$$

514 for which $n_\psi = N$ and more specifically $g^{(1)}$ and $g^{(2)}$ that
515 are illustrated in Figs. 1a, 1b.516 *Remark 2* The WT of a signal f with $g^{(N)}$ (Eq. (10)) takes
517 the following simple expression:

518
$$\begin{aligned} T_{g^{(N)}}[f](x, a) &= \frac{1}{a} \int_{-\infty}^{+\infty} f(y) g^{(N)}\left(\frac{y-x}{a}\right) dy, \\ &= a^N \frac{dx^N}{dx^N} T_{g^{(0)}}[f](x, a). \end{aligned} \quad (11)$$

TS3

519 Equation (11) shows that the WT computed with $g^{(N)}$ at
520 scale a is nothing but the N -th derivative of the signal $f(x)$
521 smoothed by a dilated version $g^{(0)}(x/a)$ of the Gaussian
522 function. This property is at the heart of various applica-
523 tions of the WT microscope as a very efficient multi-scale
524 singularity tracking technique [20].525 With the specific goal of disentangling the contribu-
526 tions to the nucleotide composition strand asymmetry
527 coming respectively from transcription and replication
528 processes, we will use in Sect. “A Wavelet-Based Method-
529 ology to Disentangle Transcription- and Replication-
530 Associated Strand Asymmetries Reveals a Remarkable
531 Gene Organization in the Human Genome”, an adapted
532 analyzing wavelet of the following form (Fig. 1c) [101,114]:
533

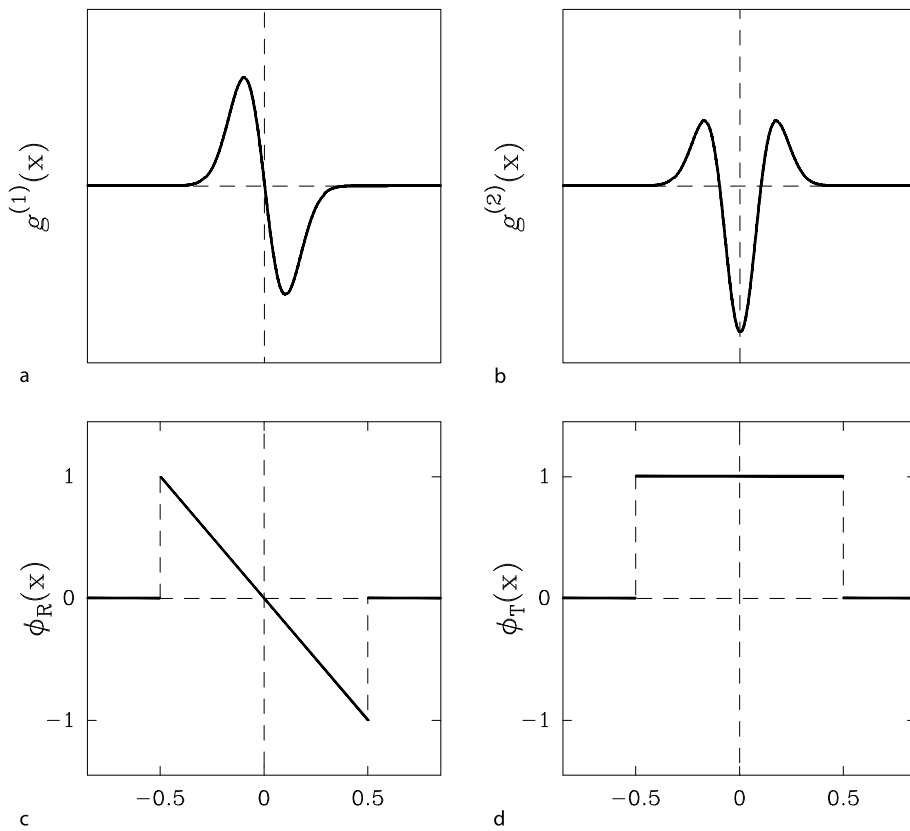
534
$$\begin{aligned} \phi_R(x) &= -\left(x - \frac{1}{2}\right), \quad \text{for } x \in \left[-\frac{1}{2}, \frac{1}{2}\right] \\ &= 0 \quad \text{elsewhere.} \end{aligned} \quad (12)$$

535 By performing multi-scale pattern recognition in the
536 (space, scale) half-plane with this analyzing wavelet, we
537 will be able to define replication domains bordered by put-
538 tative replication origins in the human genome and more
539 generally in mammalian genomes [101,114].540

Test Applications of the WTMM Method on Mono- 541 fractal and Multifractal Synthetic Random Signals

542 This section is devoted to test applications of the WTMM
543 method to random functions generated either by *additive*
544 models like fractional Brownian motions [115] or by
545 *multiplicative* models like random \mathcal{W} -cascades on wavelet
546 dyadic trees [21,22,116,117]. For each model, we first
547 wavelet transform 1000 realizations of length $L = 65536$
548 with the first order ($n_\psi = 1$) analyzing wavelet $g^{(1)}$. From
549 the WT skeletons defined by the WTMM, we compute the
550 mean partition function (Eq. (7)) from which we extract
551 the annealed $\tau(q)$ (Eq. (8)) and, in turn, $D(h)$ (Eq. (9))
552 multifractal spectra. We systematically test the robustness
553 of our estimates with respect to some change of the shape
554 of the analyzing wavelet, in particular when increasing
555 the number n_ψ of zero moments, going from $g^{(1)}$ to $g^{(2)}$
556 (Eq. (10)).557 **Fractional Brownian Signals** Since its introduction by
558 Mandelbrot and van Ness [115], the fractional Brownian
559 motion (fBm) B_H has become a very popular model in
560 signal and image processing [16,20,39]. In 1D, fBm has
561 proved useful for modeling various physical phenomena
562 with long-range dependence, e. g., “ $1/f$ ” noises. The fBm
563

TS3 Please check end of remark.



Fractals and Wavelets, Figure 1

Set of analyzing wavelets $\psi(x)$ that can be used in Eq. (1). a $g^{(1)}$ and b $g^{(2)}$ as defined in Eq. (10). c ϕ_R as defined in Eq. (12), that will be used in Sect. "A Wavelet-Based Methodology to Disentangle Transcription- and Replication-Associated Strand Asymmetries Reveals a Remarkable Gene Organization in the Human Genome" to detect replication domains. d Box function ϕ_T that will be used in Sect. "A Wavelet-Based Methodology to Disentangle Transcription- and Replication-Associated Strand Asymmetries Reveals a Remarkable Gene Organization in the Human Genome" to model step-like skew profiles induced by transcription

563 exhibits a power spectral density $S(k) \sim 1/k^\beta$, where the
 564 spectral exponent $\beta = 2H + 1$ is related to the Hurst ex-
 565 ponent H . fBm has been extensively used as test sto-
 566 chastic signals for Hurst exponent measurements. In Figs. 2, 3
 567 and 4, we report the results of a statistical analysis of fBm's
 568 using the WTMM method [12,13,14,15,16]. We mainly
 569 concentrate on $B_{1/3}$ since it has a $k^{-5/3}$ power-spectrum
 570 similar to the spectrum of the multifractal stochastic sig-
 571 nal we will study next. Actually, our goal is to demon-
 572 strate that, where the power spectrum analysis fails, the
 573 WTMM method succeeds in discriminating unambigu-
 574 ously between these two fractal signals. The numerical
 575 signals were generated by filtering uniformly generated
 576 pseudo-random noise in Fourier space in order to have the
 577 required $k^{-5/3}$ spectral density. A $B_{1/3}$ fractional Brownian
 578 trail is shown in Fig. 2a. Figure 2c illustrates the WT coded,
 579 independently at each scale a , using 256 colors. The ana-
 580 lyzing wavelet is $g^{(1)}$ ($n_\psi = 1$). Figure 3a displays some

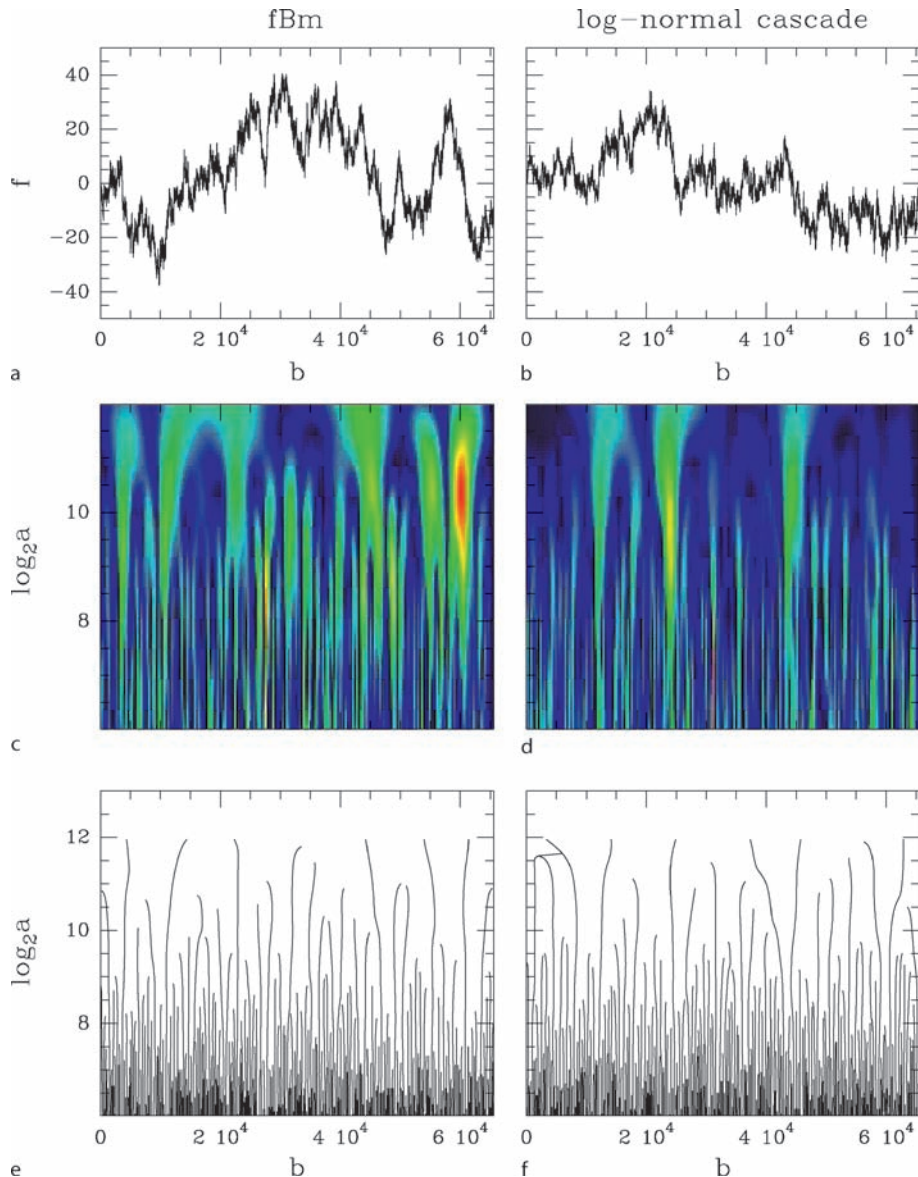
plots of $\log_2 Z(q, a)$ versus $\log_2(a)$ for different values of q ,
 581 where the partition function $Z(q, a)$ has been computed
 582 on the WTMM skeleton shown in Fig. 2e, according to the
 583 definition (Eq. (7)). Using a linear regression fit, we then
 584 obtain the slopes $\tau(q)$ of these graphs. As shown in Fig. 3c,
 585 when plotted versus q , the data for the exponents $\tau(q)$ con-
 586 sistently fall on a straight line that is remarkably fitted by
 587 the theoretical prediction:
 588

$$\tau(q) = qH - 1, \quad (13)$$

589 with $H = 1/3$. From the Legendre transform of this linear
 590 $\tau(q)$ (Eq. (9)), one gets a $D(h)$ singularity spectrum that
 591 reduces to a single point:
 592

$$D(h) = 1 \quad \text{if } h = H, \\ = -\infty \quad \text{if } h \neq H. \quad (14)$$

593 Thus, as expected theoretically [16,115], one finds that the
 594 fBm $B_{1/3}$ is a nowhere differentiable homogeneous frac-
 595



Fractals and Wavelets, Figure 2

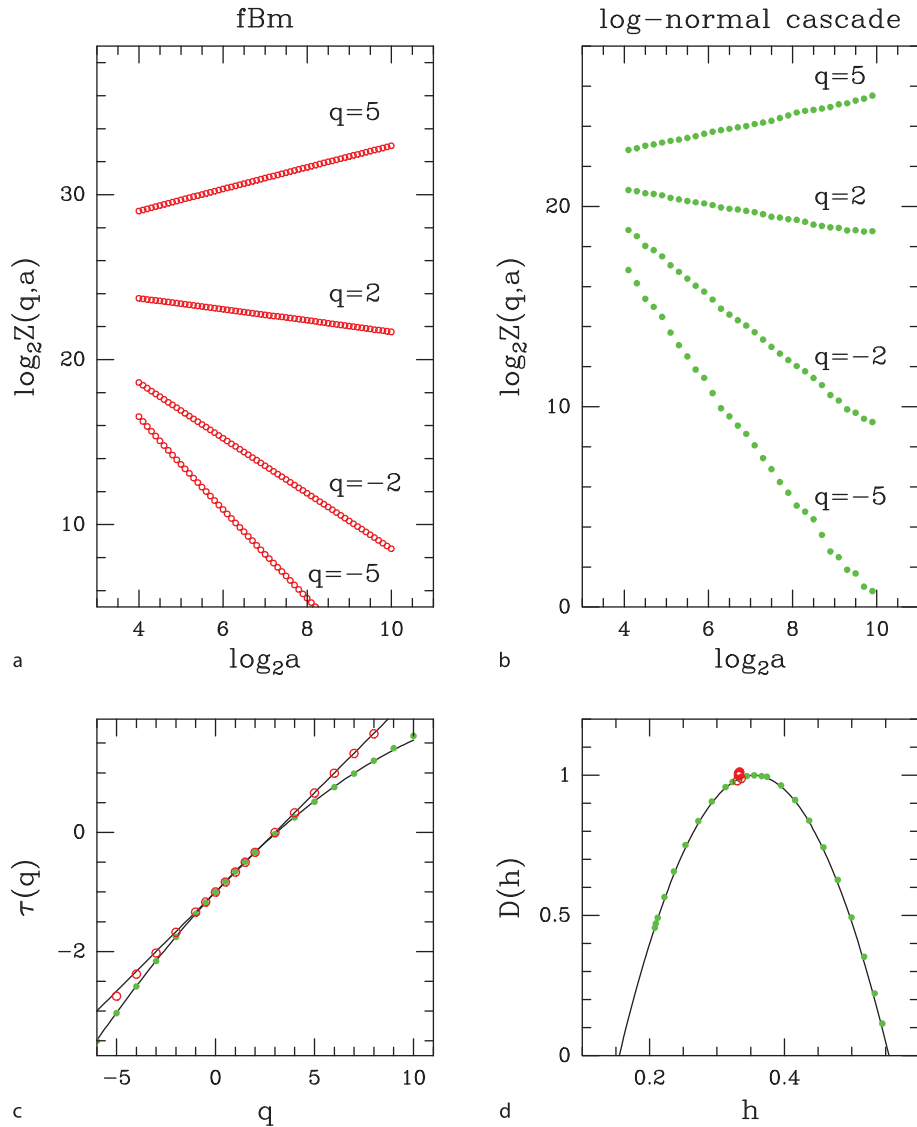
WT of monofractal and multifractal stochastic signals. *Fractional Brownian motion*: **a** a realization of $B_{1/3}$ ($L = 65536$); **c** WT of $B_{1/3}$ as coded, independently at each scale a , using 256 colors from black ($|T_{\psi}| = 0$) to red ($\max_b |T_{\psi}|$); **e** WT skeleton defined by the set of all the maxima lines. *Log-normal random W-cascades*: **b** a realization of the log-normal W-cascade model ($L = 65536$) with the following parameter values $m = -0.355 \ln 2$ and $\sigma^2 = 0.02 \ln 2$ (see [116]); **d** WT of the realization in **b** represented with the same color coding as in **c**; **f** WT skeleton. The analyzing wavelet is $g^{(1)}$ (see Fig. 1a)

596 tal signal with a unique Hölder exponent $h = H = 1/3$.
 597 Note that similar good estimates are obtained when using
 598 analyzing wavelets of different order (e.g. $g^{(2)}$), and this
 599 whatever the value of the index H of the fBm [12,13,14,15,
 600 16].

601 Within the perspective of confirming the monofractal-
 602 ity of fBm's, we have studied the probability density func-

603 tion (pdf) of wavelet coefficient values $\rho_a(T_{g^{(1)}}(., a))$, as
 604 computed at a fixed scale a in the fractal scaling range. Ac-
 605 cording to the monofractal scaling properties, one expects
 606 these pdfs to satisfy the self-similarity relationship [20,27,
 607 28]:

$$608 a^H \rho_a(a^H T) = \rho(T) , \quad (15)$$



Fractals and Wavelets, Figure 3

Determination of the $\tau(q)$ and $D(h)$ multifractal spectra of fBm $B_{1/3}$ (red circles) and log-normal random \mathcal{W} -cascades (green dots) using the WTMM method. **a.** $\log_2 Z(q, a)$ vs. $\log_2 a$: $B_{1/3}$. **b.** $\log_2 Z(q, a)$ vs. $\log_2 a$: Log-normal \mathcal{W} -cascades with the same parameters as in Fig. 2b. **c.** $\tau(q)$ vs. q ; the solid lines correspond respectively to the theoretical spectra (13) and (16). **d.** $D(h)$ vs. h ; the solid lines correspond respectively to the theoretical predictions (14) and (17). The analyzing wavelet is $g^{(1)}$. The reported results correspond to annealed averaging over 1000 realizations of $L = 65\,536$

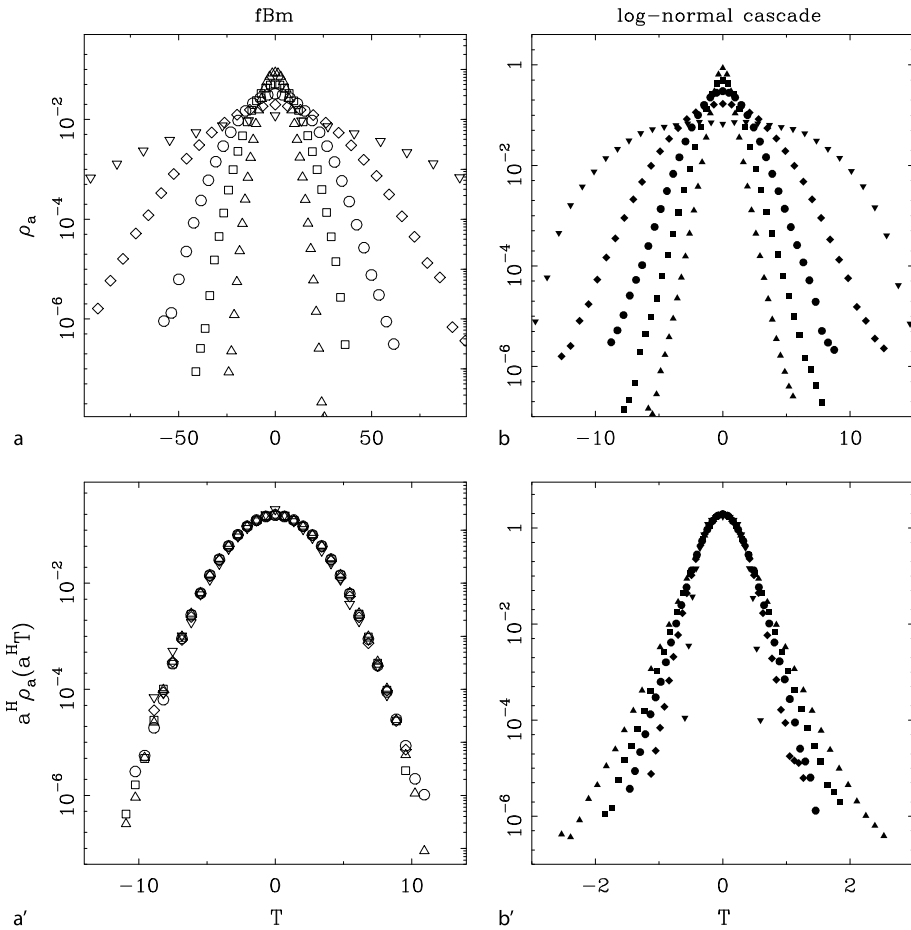
609 where $\rho(T)$ is a “universal” pdf (actually the pdf obtained
 610 at scale $a = 1$) that does not depend on the scale parameter a . As shown in Figs. 4a, 4a' for $B_{1/3}$, when plotting
 611 $a^H \rho_a(a^H T)$ vs. T , all the ρ_a curves corresponding to different scales (Fig. 4a) remarkably collapse on a unique
 612 curve when using a unique exponent $H = 1/3$ (Fig. 4a'). Furthermore the so-obtained universal curve cannot be
 613 distinguished from a parabola in semi-log representation
 614

615 as the signature of the monofractal Gaussian statistics of
 616 fBm fluctuations [16,20,27].

617 **Random \mathcal{W} -Cascades** Multiplicative cascade models
 618 have enjoyed increasing interest in recent years as the paradigm of multifractal objects [16,19,48,105,107,108,
 619 118]. The notion of cascade actually refers to a self-simil-
 620 ar process whose properties are defined multiplicatively
 621

617
 618

619
 620
 621
 622
 623



Fractals and Wavelets, Figure 4

Probability distribution functions of wavelet coefficient values of fBm $B_{1/3}$ (open symbols) and log-normal random \mathcal{W} -cascades (filled symbols) with the same parameters as in Fig. 2b. a ρ_a vs. $T_{g^{(1)}}$ for the set of scales $a = 10 (\Delta), 50 (\square), 100 (\bigcirc), 1000 (\diamond), 9000 (\nabla)$; $a^H \rho_a(\rho(a^H T_{g^{(1)}}))$ vs. $T_{g^{(1)}}$ with $H = 1/3$; The symbols have the same meaning as in a. b ρ_a vs. $T_{g^{(1)}}$ for the set of scales $a = 10 (\blacktriangle), 50 (\blacksquare), 100 (\bullet), 1000 (\blacklozenge), 9000 (\blacktriangledown)$; (b') $a^H \rho_a(a^H T_{g^{(1)}})$ vs. $T_{g^{(1)}}$ with $H = -m/\ln 2 = 0.355$. The analyzing wavelet is $g^{(1)}$ (Fig. 1a)

from coarse to fine scales. In that respect, it occupies a central place in the statistical theory of turbulence [48,104]. Originally, the concept of self-similar cascades was introduced to model multifractal measures (e. g. dissipation or enstrophy) [48]. It has been recently generalized to the construction of scale-invariant signals (e. g. longitudinal velocity, pressure, temperature) using orthogonal wavelet basis [116,119]. Instead of redistributing the measure over sub-intervals with multiplicative weights, one allocates the wavelet coefficients in a multiplicative way on the dyadic grid. This method has been implemented to generate multifractal functions (with weights W) from a given deterministic or probabilistic multiplicative process. Along the line of the modeling of fully developed turbulent signals by log-infinitely divisible multiplicative processes [120,121],

we will mainly concentrate here on the log-normal \mathcal{W} -cascades in order to calibrate the WTMM method. If m and σ^2 are respectively the mean and the variance of $\ln W$ (where W is a multiplicative random variable with log-normal probability distribution), then, as shown in [116], a straightforward computation leads to the following $\tau(q)$ spectrum:

$$\begin{aligned} \tau(q) &= -\log_2 \langle W^q \rangle - 1, \quad \forall q \in \mathbb{R} \\ &= -\frac{\sigma^2}{2 \ln 2} q^2 - \frac{m}{\ln 2} q - 1, \end{aligned} \quad (16)$$

where $\langle \dots \rangle$ means ensemble average. The corresponding $D(h)$ singularity spectrum is obtained by Legendre

649 transforming $\tau(q)$ (Eq. (9)):

$$650 \quad D(h) = -\frac{(h + m/\ln 2)^2}{2\sigma^2/\ln 2} + 1. \quad (17)$$

651 According to the convergence criteria established
 652 in [116], m and σ^2 have to satisfy the conditions: $m < 0$
 653 and $|m|/\sigma > \sqrt{2 \ln 2}$. Moreover, by solving $D(h) = 0$, one
 654 gets the following bounds for the support of the $D(h)$ sing-
 655 ularity spectrum: $h_{\min} = -m/\ln 2 - (\sqrt{2}\sigma)/\sqrt{\ln 2}$ and
 656 $h_{\max} = -m/\ln 2 + (\sqrt{2}\sigma)/\sqrt{\ln 2}$.

657 In Fig. 2b is illustrated a realization of a log-normal
 658 \mathcal{W} -cascade for the parameter values $m = -0.355 \ln 2$ and
 659 $\sigma^2 = 0.02 \ln 2$. The corresponding WT and WT skeleton
 660 as computed with $g^{(1)}$ are shown in Figs. 2d and 2f re-
 661 spectively. The results of the application of the WTMM
 662 method are reported in Fig. 3. As shown in Fig. 3b, when
 663 plotted versus the scale parameter a in a logarithmic rep-
 664 resentation, the annealed average of the partition func-
 665 tions $Z(q, a)$ displays a well defined scaling behavior over
 666 a range of scales of about 5 octaves. Note that scaling
 667 of quite good quality is found for a rather wide range
 668 of q values: $-5 \leq q \leq 10$. When processing to a linear
 669 regression fit of the data over the first four octaves, one
 670 gets the $\tau(q)$ spectrum shown in Fig. 3c. This spectrum
 671 is clearly a nonlinear function of q , the hallmark of mul-
 672 tifractal scaling. Moreover, the numerical data are in re-
 673 markable agreement with the theoretical quadratic predic-
 674 tion (Eq. (16)). Similar quantitative agreement is observed
 675 on the $D(h)$ singularity spectrum in Fig. 3d which displays
 676 a single humped parabola shape that characterizes inter-
 677 mittent fluctuations corresponding to Hölder exponents
 678 values ranging from $h_{\min} = 0.155$ to $h_{\max} = 0.555$. Un-
 679 fortunately, to capture the strongest and the weakest sin-
 680 gularities, one needs to compute the $\tau(q)$ spectrum for
 681 very large values of $|q|$. This requires the processing of
 682 many more realizations of the considered log-normal ran-
 683 dom \mathcal{W} -cascade. The multifractal nature of log-normal
 684 \mathcal{W} -cascade realizations is confirmed in Figs. 4b, 4b' where
 685 the self-similarity relationship (Eq. (15)) is shown not to
 686 apply. Actually there does not exist a H value allowing to
 687 superimpose onto a single curve the WT pdfs computed at
 688 different scales.

689 The test applications reported in this section demon-
 690 strate the ability of the WTMM method to resolve mul-
 691 tifractal scaling of 1D signals, a hopeless task for classi-
 692 cal power spectrum analysis. They were used on purpose
 693 to calibrate and to test the reliability of our methodology,
 694 and of the corresponding numerical tools, with respect to
 695 finite-size effects and statistical convergence.

Bifractality of Human DNA Strand-Asymmetry Profiles Results from Transcription

696

697

698 During genome evolution, mutations do not occur at ran-
 699 dom as illustrated by the diversity of the nucleotide sub-
 700stitution rate values [122,123,124,125]. This non-random-
 701ness is considered as a by-product of the various DNA
 702 mutation and repair processes that can affect each of the
 703 two DNA strands differently. Asymmetries of substitution
 704 rates coupled to transcription have been mainly observed
 705 in prokaryotes [88,89,91], with only preliminary results in
 706 eukaryotes. In the human genome, excess of T was ob-
 707 served in a set of gene introns [126] and some large-scale
 708 asymmetry was observed in human sequences but they
 709 were attributed to replication [127]. Only recently, a com-
 710 parative analysis of mammalian sequences demonstrated
 711 a transcription-coupled excess of G+T over A+C in the
 712 coding strand [95,96,97]. In contrast to the substitution
 713 biases observed in bacteria presenting an excess of C→T
 714 transitions, these asymmetries are characterized by an ex-
 715 cess of purine (A→G) transitions relatively to pyrimidine
 716 (T→C) transitions. These might be a by-product of the
 717 transcription-coupled repair mechanism acting on uncor-
 718 rected substitution errors during replication [128]. In this
 719 section, we report the results of a genome-wide multifrac-
 720 tal analysis of strand-asymmetry DNA walk profiles in the
 721 human genome [129]. This study is based on the compu-
 722 tation of the TA and GC skews in non-overlapping 1 kbp
 723 windows:

$$724 \quad S_{TA} = \frac{n_T - n_A}{n_T + n_A}, \quad S_{GC} = \frac{n_G - n_C}{n_G + n_C}, \quad (18)$$

725 where n_A , n_C , n_G and n_T are respectively the numbers of
 726 A, C, G and T in the windows. Because of the observed cor-
 727 relation between the TA and GC skews, we also considered
 728 the total skew

$$729 \quad S = S_{TA} + S_{GC}. \quad (19)$$

730 From the skews $S_{TA}(n)$, $S_{GC}(n)$ and $S(n)$, obtained along
 731 the sequences, where n is the position (in kbp units) from
 732 the origin, we also computed the cumulative skew profiles
 733 (or skew walk profiles):

$$734 \quad \Sigma_{TA}(n) = \sum_{j=1}^n S_{TA}(j), \quad \Sigma_{GC}(n) = \sum_{j=1}^n S_{GC}(j), \quad (20)$$

735 and

$$736 \quad \Sigma(n) = \sum_{j=1}^n S(j). \quad (21)$$

737 Our goal is to show that the skew DNA walks of the
 738 22 human autosomes display an unexpected (with respect

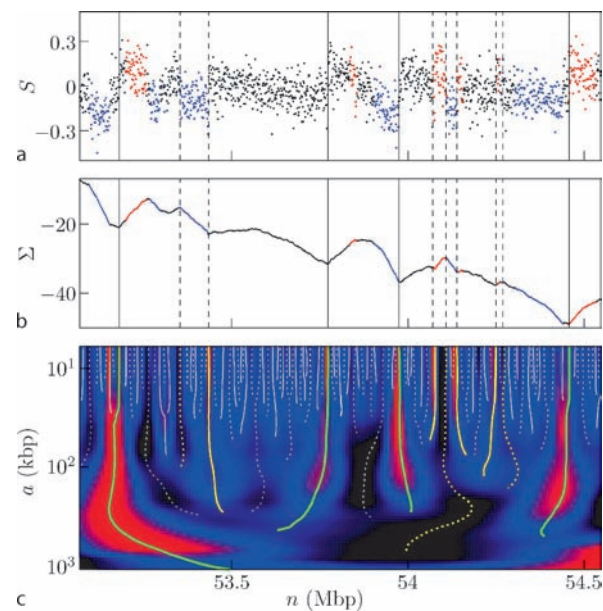
739 to previous monofractal diagnosis [27,28,29,30]) bifractal
 740 scaling behavior in the range 10 to 40 kbp as the signature
 741 of the presence of transcription-induced jumps in the LRC
 742 noisy S profiles. Sequences and gene annotation data (“ref-
 743 Gene”) were retrieved from the UCSC Genome Browser
 744 (May 2004). We used RepeatMasker to exclude repetitive
 745 elements that might have been inserted recently and would
 746 not reflect long-term evolutionary patterns.

747 **Revealing the Bifractality of Human Skew DNA Walks
 748 with the WTMM Method**

749 As an illustration of our wavelet-based methodology, we
 750 show in Fig. 5 the S skew profile of a fragment of human
 751 chromosome 6 (Fig. 5a), the corresponding skew DNA
 752 walk (Fig. 5b) and its space-scale wavelet decomposition
 753 using the Mexican hat analyzing wavelet $g^{(2)}$ (Fig. 1b).
 754 When computing $Z(q, a)$ (Eq. (7)) from the WT skeletons
 755 of the skew DNA walks Σ of the 22 human autosomes,
 756 we get convincing power-law behavior for $-1.5 \leq q \leq 3$
 757 (data not shown). In Fig. 6a are reported the $\tau(q)$ ex-
 758ponents obtained using a linear regression fit of $\ln Z(q, a)$
 759 vs. $\ln a$ over the range of scales $10 \text{ kbp} \leq a \leq 40 \text{ kbp}$.
 760 All the data points remarkably fall on two straight lines
 761 $\tau_1(q) = 0.78q - 1$ and $\tau_2(q) = q - 1$ which strongly sug-
 762 gests the presence of two types of singularities $h_1 = 0.78$
 763 and $h_2 = 1$, respectively on two sets S_1 and S_2 with the
 764 same Hausdorff dimension $D = -\tau_1(0) = -\tau_2(0) = 1$, as
 765 confirmed when computing the $D(h)$ singularity spectrum
 766 in Fig. 6b. This observation means that $Z(q, a)$ can be split
 767 in two parts [12,16]:

$$768 Z(q, a) = C_1(q)a^{q h_1 - 1} + C_2(q)a^{q h_2 - 1}, \quad (22)$$

769 where $C_1(q)$ and $C_2(q)$ are prefactors that depend on q .
 770 Since $h_1 < h_2$, in the limit $a \mapsto 0^+$, the partition function
 771 is expected to behave like $Z(q, a) \sim C_1(q)a^{q h_1 - 1}$ for $q > 0$
 772 and like $Z(q, a) \sim C_2(q)a^{q h_2 - 1}$ for $q < 0$, with a so-called
 773 phase transition [12,16] at the critical value $q_c = 0$. Sur-
 774 prisingly, it is the contribution of the weakest singularities
 775 $h_2 = 1$ that controls the scaling behavior of $Z(q, a)$ for
 776 $q > 0$ while the strongest ones $h_1 = 0.78$ actually domi-
 777 nate for $q < 0$ (Fig. 6a). This inverted behavior originates
 778 from finite (1 kbp) resolution which prevents the observa-
 779 tion of the predicted scaling behavior in the limit $a \mapsto 0^+$.
 780 The prefactors $C_1(q)$ and $C_2(q)$ in Eq. (22) are sensitive to
 781 (i) the number of maxima lines in the WT skeleton along
 782 which the WTMM behave as a^{h_1} or a^{h_2} and (ii) the rela-
 783 tive amplitude of these WTMM. Over the range of scales
 784 used to estimate $\tau(q)$, the WTMM along the maxima lines
 785 pointing (at small scale) to $h_2 = 1$ singularities are signifi-
 786 cantly larger than those along the maxima lines associated

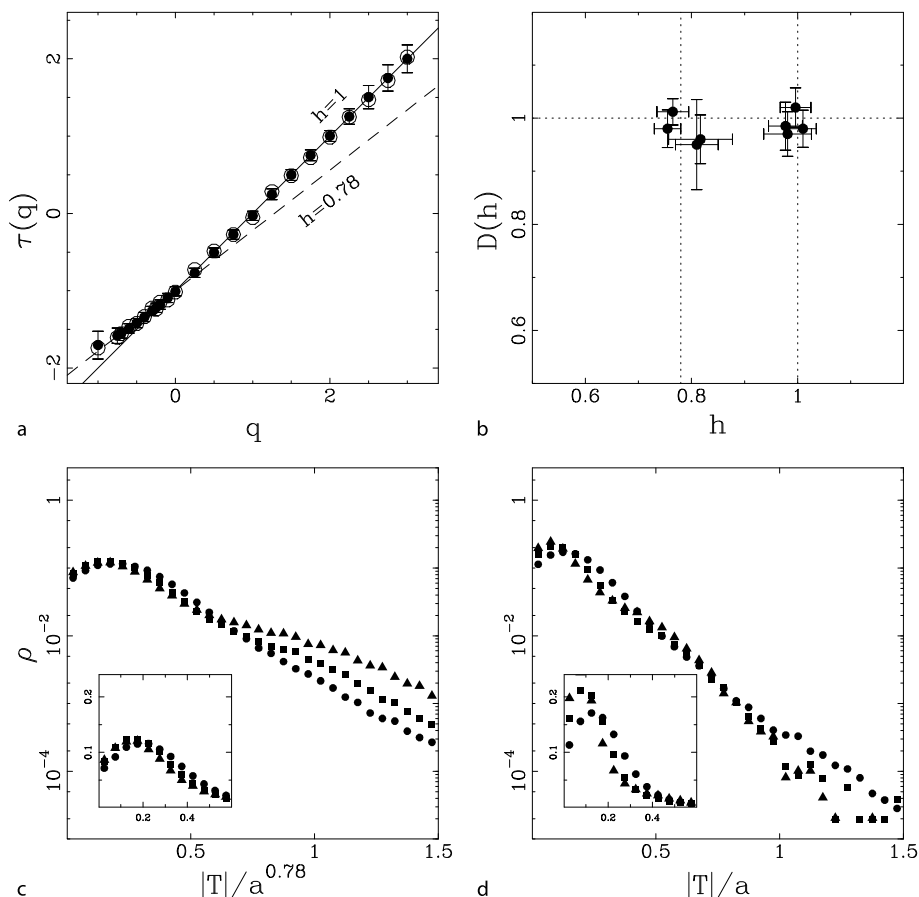


Fractals and Wavelets, Figure 5

a Skew profile $S(n)$ (Eq. (19)) of a repeat-masked fragment of human chromosome 6; red (resp. blue) 1 kbp window points correspond to (+) genes (resp. (-) genes) lying on the Watson (resp. Crick) strand; black points to intergenic regions. b Cumulated skew profile $\Sigma(n)$ (Eq. (21)). c WT of Σ ; $T_{g^{(2)}}(n, a)$ is coded from black (min) to red (max); the WT skeleton defined by the maxima lines is shown in solid (resp. dashed) lines corresponding to positive (resp. negative) WT values. For illustration yellow solid (resp. dashed) maxima lines are shown to point to the positions of 2 upward (resp. 2 downward) jumps in S (vertical dashed lines in a and b) that coincide with gene transcription starts (resp. ends). In green are shown maxima lines that persist above $a \geq 200$ kbp and that point to sharp upward jumps in S (vertical solid lines in a and b) that are likely to be the locations of putative replication origins (see Sect. “From the Detection of Relocation Origins Using the Wavelet Transform Microscope to the Modeling of Replication in Mammalian Genomes”) [98,100]; note that 3 out of those 4 jumps are co-located with transcription start sites [129]

787 to $h_1 = 0.78$ (see Figs. 6c, 6d). This implies that the larger
 788 $q > 0$, the stronger the inequality $C_2(q) \gg C_1(q)$ and the
 789 more pronounced the relative contribution of the second
 790 term in the r.h.s. of Eq. (22). On the opposite for $q < 0$,
 791 $C_1(q) \gg C_2(q)$ which explains that the strongest singular-
 792 ities $h_1 = 0.78$ now control the scaling behavior of $Z(q, a)$
 793 over the explored range of scales.

794 In Figs. 6c, 6d are shown the WTMM pdfs computed
 795 at scales $a = 10, 20$ and 40 kbp after rescaling by a^{h_1} and
 796 a^{h_2} respectively. We note that there does not exist a value
 797 of H such that all the pdfs collapse on a single curve as
 798 expected from Eq. (15) for monofractal DNA walks. Con-
 799 sistently with the $\tau(q)$ data in Fig. 6a and with the in-



Fractals and Wavelets, Figure 6

Multifractal analysis of $\Sigma(n)$ of the 22 human (filled symbols) and 19 mouse (open circle) autosomes using the WTMM method with $g^{(2)}$ over the range $10 \text{ kbp} \leq a \leq 40 \text{ kbp}$ [129]. **a** $\tau(q)$ vs. q . **b** $D(h)$ vs. h . **c** WTMM pdf: ρ is plotted versus $|T|/a^H$ where $H = h_1 = 0.78$, in semi-log representation; the inset is an enlargement of the pdf central part in linear representation. **d** Same as in **c** but with $H = h_2 = 1$. In **c** and **d**, the symbols correspond to scales $a = 10$ (●), 20 (■) and 40 kbp (▲)

verted scaling behavior discussed above, when using the two exponents $h_1 = 0.78$ and $h_2 = 1$, one succeeds in superimposing respectively the central (bump) part (Fig. 6c) and the tail (Fig. 6d) of the rescaled WTMM pdfs. This corroborates the bifractal nature of the skew DNA walks that display two competing scale-invariant components of Hölder exponents: (i) $h_1 = 0.78$ corresponds to LRC homogeneous fluctuations previously observed over the range $200 \text{ bp} \lesssim a \lesssim 20 \text{ kbp}$ in DNA walks generated with structural codings [29,30] and (ii) $h_2 = 1$ is associated to convex \vee and concave \wedge shapes in the DNA walks Σ indicating the presence of discontinuities in the derivative of Σ , i. e., of jumps in S (Figs. 5a, 5b). At a given scale a , according to Eq. (11), a large value of the WTMM in Fig. 5c corresponds to a strong derivative of the smoothed S profile and the maxima line to which it belongs is likely to

point to a jump location in S . This is particularly the case for the colored maxima lines in Fig. 5c: Upward (resp. downward) jumps (Fig. 5a) are so-identified by the maxima lines corresponding to positive (resp. negative) values of the WT.

Transcription-Induced Step-Like Skew Profiles in the Human Genome

In order to identify the origin of the jumps observed in the skew profiles, we have performed a systematic investigation of the skews observed along 14 854 intron containing genes [96,97]. In Fig. 7 are reported the mean values of S_{TA} and S_{GC} skews for all genes as a function of the distance to the 5'- or 3'- end. At the 5' gene extremities (Fig. 7a), a sharp transition of both skews is observed

816

817

818

819

820

821

822

823

824

825

826

827

828

829

830 from about zero values in the intergenic regions to finite
 831 positive values in transcribed regions ranging between 4
 832 and 6% for \bar{S}_{TA} and between 3 and 5% for \bar{S}_{GC} . At the
 833 gene 3'- extremities (Fig. 7b), the TA and GC skews also
 834 exhibit transitions from significantly large values in trans-
 835cribed regions to very small values in untranscribed re-
 836gions. However, in comparison to the steep transitions ob-
 837 served at 5'- ends, the 3'- end profiles present a slightly
 838 smoother transition pattern extending over ~ 5 kbp and
 839 including regions downstream of the 3'- end likely reflect-
 840 ing the fact that transcription continues to some extent
 841 downstream of the polyadenylation site. In pluricellular
 842 organisms, mutations responsible for the observed biases
 843 are expected to have mostly occurred in germ-line cells. It
 844 could happen that gene 3'- ends annotated in the databank
 845 differ from the poly-A sites effectively used in the germ-
 846 line cells. Such differences would then lead to some broad-
 847 ening of the skew profiles.

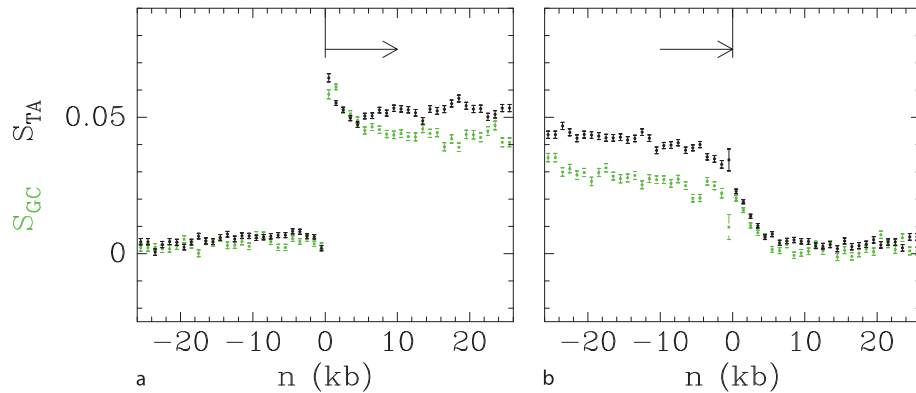
848 From Skew Multifractal Analysis to Gene Detection

849 In Fig. 8 are reported the results of a statistical analysis
 850 of the jump amplitudes in human S profiles [129]. For
 851 maxima lines that extend above $a^* = 10$ kbp in the WT
 852 skeleton (see Fig. 5c), the histograms obtained for up-
 853 ward and downward variations are quite similar, especially
 854 their tails that are likely to correspond to jumps in the S
 855 profiles (Fig. 8a). When computing the distance between
 856 upward or downward jumps ($|\Delta S| \geq 0.1$) to the closest
 857 transcription start (TSS) or end (TES) sites (Fig. 8b), we
 858 reveal that the number of upward jumps in close prox-
 859 imity ($|\Delta n| \lesssim 3$ kbp) to TSS over-exceeds the number of
 860 such jumps close to TES. Similarly, downward jumps are
 861 preferentially located at TES. These observations are con-
 862 sistent with the step-like shape of skew profiles induced
 863 by transcription: $S > 0$ (resp. $S < 0$) is constant along
 864 a (+) (resp. (-)) gene and $S = 0$ in the intergenic regions
 865 (Fig. 7) [96]. Since a step-like pattern is edged by one up-
 866 ward and one downward jump, the set of human genes
 867 that are significantly biased is expected to contribute to an
 868 even number of $\Delta S > 0$ and $\Delta S < 0$ jumps when explor-
 869 ing the range of scales $10 \lesssim a \lesssim 40$ kbp, typical of human
 870 gene size. Note that in Fig. 8a, the number of sharp upward
 871 jumps actually slightly exceeds the number of sharp down-
 872 ward jumps, consistently with the experimental observa-
 873 tion that whereas TSS are well defined, TES may extend
 874 over 5 kbp resulting in smoother downward skew transi-
 875 tions (Fig. 7b). This TES particularity also explains the ex-
 876 cess of upward jumps found close to TSS as compared to
 877 the number of downward jumps close to TES (Fig. 8b).

878 In Fig. 9a, we report the analysis of the distance of
 879 TSS to the closest upward jump [129]. For a given up-
 880 ward jump amplitude, the number of TSS with a jump
 881 within $|\Delta n|$ increases faster than expected (as compared
 882 to the number found for randomized jump positions) up
 883 to $|\Delta n| \simeq 2$ kbp. This indicates that the probability to find
 884 an upward jump within a gene promoter region is signif-
 885 icantly larger than elsewhere. For example, out of 20 023
 886 TSS, 36% (7228) are delineated within 2 kbp by a jump
 887 with $\Delta S > 0.1$. This provides a very reasonable estimate
 888 for the number of genes expressed in germline cells as
 889 compared to the 31.9% recently experimentally found to
 890 be bound to Pol II in human embryonic stem cells [130].

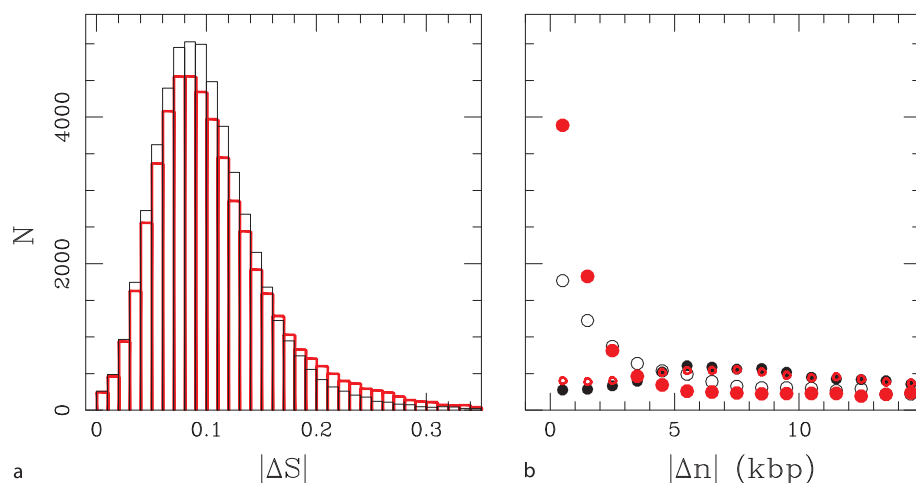
891 Combining the previous results presented in Figs. 8b
 892 and 9a, we report in Fig. 9b an estimate of the effi-
 893 ciency/coverage relationship by plotting the proportion
 894 of upward jumps ($\Delta S > \Delta S^*$) lying in TSS proximity as
 895 a function of the number of so-delineated TSS [129]. For
 896 a given proximity threshold $|\Delta n|$, increasing ΔS^* results
 897 in a decrease of the number of delineated TSS, charac-
 898 teristic of the right tail of the gene bias pdf. Concomi-
 899 tant to this decrease, we observe an increase of the effi-
 900 ciency up to a maximal value corresponding to some opti-
 901 mal value for ΔS^* . For $|\Delta n| < 2$ kbp, we reach a maximal
 902 efficiency of 60% for $\Delta S^* = 0.225$; 1403 out of 2342 up-
 903 ward jumps delineate a TSS. Given the fact that the actual
 904 number of human genes is estimated to be significantly
 905 larger ($\sim 30\,000$) than the number provided by refGene,
 906 a large part of the the 40% (939) of upward jumps that have
 907 not been associated to a refGene could be explained by this
 908 limited coverage. In other words, jumps with sufficiently
 909 high amplitude are very good candidates for the location
 910 of highly-biased gene promoters. Let us point that out of
 911 the above 1403 (resp. 2342) upward jumps, 496 (resp. 624)
 912 jumps are still observed at scale $a^* = 200$ kbp. We will
 913 see in the next section that these jumps are likely to also
 914 correspond to replication origins underlying the fact that
 915 large upward jumps actually result from the cooperative
 916 contributions of both transcription- and replication- as-
 917 sociated biases [98,99,100,101]. The observation that 80%
 918 (496/624) of the predicted replication origins are co-loc-
 919 ated with TSS enlightens the existence of a remarkable
 920 gene organization at replication origins [101].

921 To summarize, we have demonstrated the bifractal
 922 character of skew DNA walks in the human genome.
 923 When using the WT microscope to explore (repeat-
 924 masked) scales ranging from 10 to 40 kbp, we have iden-
 925 tified two competing homogeneous scale-invariant com-
 926 ponents characterized by Hölder exponents $h_1 = 0.78$
 927 and $h_2 = 1$ that respectively correspond to LRC colored
 928 noise and sharp jumps in the original DNA composi-



Fractals and Wavelets, Figure 7

TA (●) and GC (green ●) skew profiles in the regions surrounding 5' and 3' gene extremities [96]. S_{TA} and S_{GC} were calculated in 1 kbp windows starting from each gene extremities in both directions. In abscissa is reported the distance (n) of each 1 kbp window to the indicated gene extremity; zero values of abscissa correspond to 5'- (a) or 3'- (b) gene extremities. In ordinate is reported the mean value of the skews over our set of 14854 intron-containing genes for all 1 kbp windows at the corresponding abscissa. Error bars represent the standard error of the means



Fractals and Wavelets, Figure 8

Statistical analysis of skew variations at the singularity positions determined at scale 1 kbp from the maxima lines that exist at scales $a \geq 10$ kbp in the WT skeletons of the 22 human autosomes [129]. For each singularity, we computed the variation amplitudes $\Delta S = \bar{S}(3') - \bar{S}(5')$ over two adjacent 5 kbp windows, respectively in the 3' and 5' directions and the distances Δn to the closest TSS (resp. TES). a Histograms $N(|\Delta S|)$ for upward ($\Delta S > 0$, red) and downward ($\Delta S < 0$, black) skew variations. b Histograms of the distances Δn of upward (red) or downward (black) jumps with $|\Delta S| \geq 0.1$ to the closest TSS (●, red ●) and TES (○, red ○)

929 tional asymmetry profiles. Remarkably, the so-identified
 930 upward (resp. downward) jumps are mainly found at the
 931 TSS (resp. TES) of human genes with high transcription
 932 bias and thus very likely highly expressed. As illustrated in
 933 Fig. 6a, similar bifractal properties are also observed when
 934 investigating the 19 mouse autosomes. This suggests that
 935 the results reported in this section are general features of
 936 mammalian genomes [129].

From the Detection of Replication Origins Using the Wavelet Transform Microscope to the Modeling of Replication in Mammalian Genomes

937

938

939

940

941

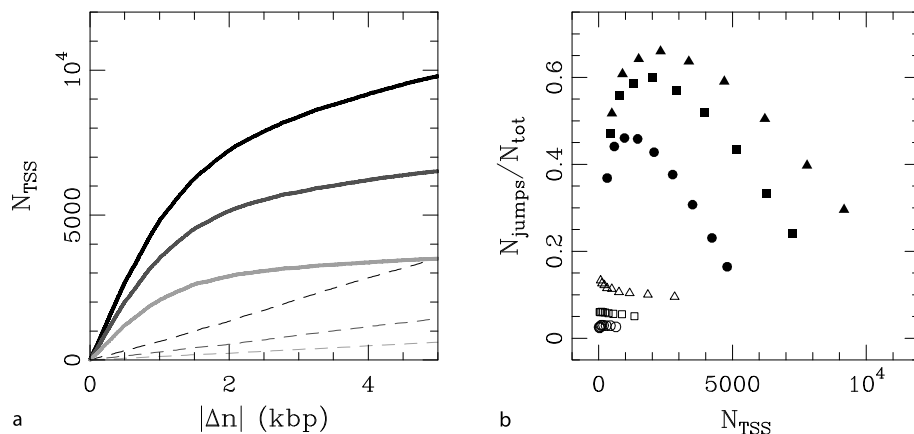
942

943

944

945

DNA replication is an essential genomic function responsible for the accurate transmission of genetic information through successive cell generations. According to the so-called “replicon” paradigm derived from prokaryotes [131], this process starts with the binding of some “initiator” protein to a specific “replicator” DNA se-



Fractals and Wavelets, Figure 9

a Number of TSS with an upward jump within $|\Delta n|$ (abscissa) for jump amplitudes $\Delta S > 0.1$ (black), 0.15 (dark gray) and 0.2 (light gray). Solid lines correspond to true jump positions while dashed lines to the same analysis when jump positions were randomly drawn along each chromosome [129]. **b** Among the $N_{\text{tot}}(\Delta S^*)$ upward jumps of amplitude larger than some threshold ΔS^* , we plot the proportion of those that are found within 1 kbp (●), 2 kbp (■) or 4 kbp (▲) of the closest TSS vs. the number N_{TSS} of the so-delimited TSS. Curves were obtained by varying ΔS^* from 0.1 to 0.3 (from right to left). Open symbols correspond to similar analyzes performed on random upward jump and TSS positions

quence called *origin of replication*. The recruitment of additional factors initiate the bi-directional progression of two divergent replication forks along the chromosome. One strand is replicated continuously (leading strand), while the other strand is replicated in discrete steps towards the origin (lagging strand). In eukaryotic cells, this event is initiated at a number of replication origins and propagates until two converging forks collide at a *terminus of replication* [132]. The initiation of different replication origins is coupled to the cell cycle but there is a definite flexibility in the usage of the replication origins at different developmental stages [133,134,135,136, 137]. Also, it can be strongly influenced by the distance and timing of activation of neighboring replication origins, by the transcriptional activity and by the local chromatin structure [133,134,135,137]. Actually, sequence requirements for a replication origin vary significantly between different eukaryotic organisms. In the unicellular eukaryote *Saccharomyces cerevisiae*, the replication origins spread over 100–150 bp and present some highly conserved motifs [132]. However, among eukaryotes, *S. cerevisiae* seems to be the exception that remains faithful to the replicon model. In the fission yeast *Schizosaccharomyces pombe*, there is no clear consensus sequence and the replication origins spread over at least 800 to 1000 bp [132]. In multicellular organisms, the nature of initiation sites of DNA replication is even more complex. Metazoan replication origins are rather poorly defined and initiation may occur at multiple sites distributed over a thousand of base pairs [138]. The initiation of replication at random and

closely spaced sites was repeatedly observed in *Drosophila* and *Xenopus* early embryo cells, presumably to allow for extremely rapid S phase, suggesting that any DNA sequence can function as a replicator [136,139,140]. A developmental change occurs around midblastula transition that coincides with some remodeling of the chromatin structure, transcription ability and selection of preferential initiation sites [136,140]. Thus, although it is clear that some sites consistently act as replication origins in most eukaryotic cells, the mechanisms that select these sites and the sequences that determine their location remain elusive in many cell types [141,142]. As recently proposed by many authors [143,144,145], the need to fulfill specific requirements that result from cell diversification may have led multicellular eukaryotes to develop various epigenetic controls over the replication origin selection rather than to conserve specific replication sequence. This might explain that only very few replication origins have been identified so far in multicellular eukaryotes, namely around 20 in metazoa and only about 10 in human [146]. Along the line of this epigenetic interpretation, one might wonder what can be learned about eukaryotic DNA replication from DNA sequence analysis.

Replication Induced Factory-Roof Skew Profiles in Mammalian Genomes

The existence of replication associated strand asymmetries has been mainly established in bacterial genomes [87,90, 92,93,94]. SGC and STA skews abruptly switch sign (over

TS4 Please check. Fig. 13 is cited before Fig. 10.

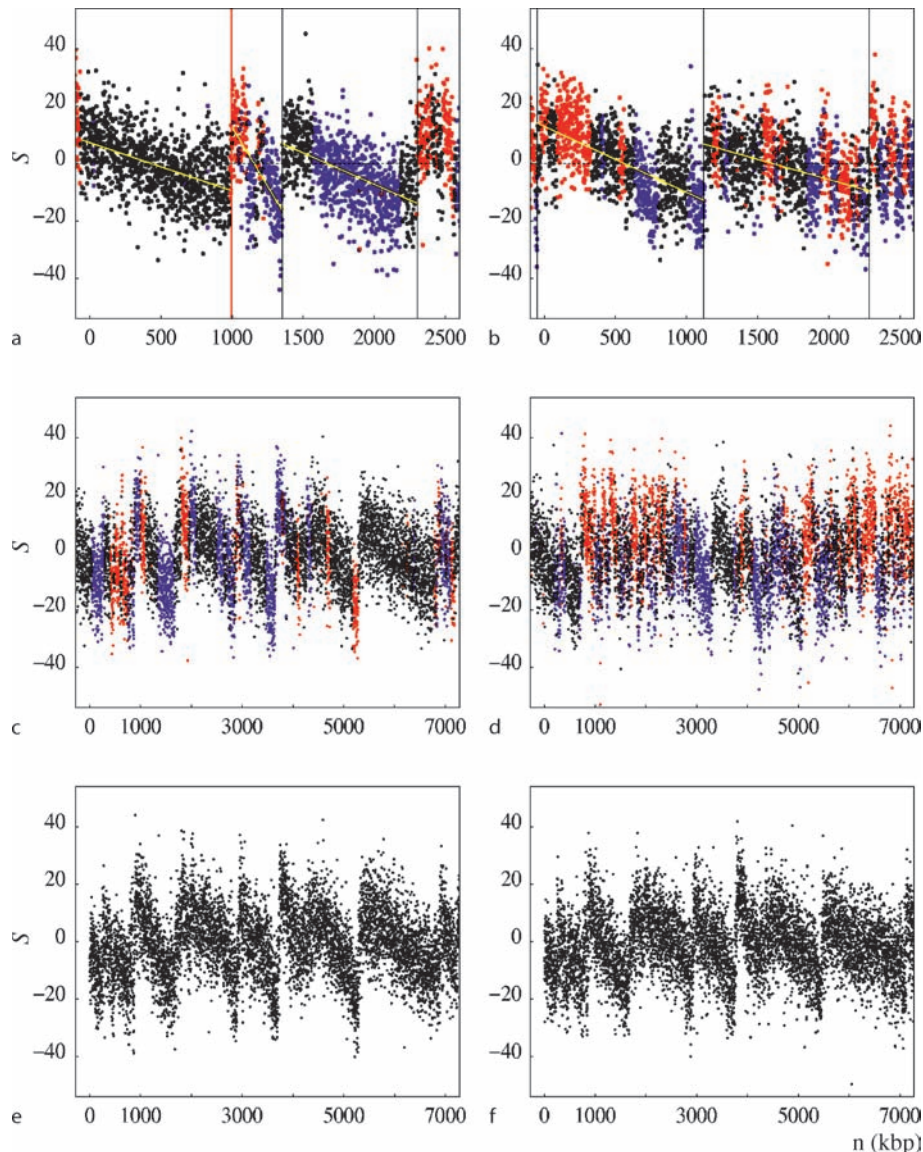
1004 few kbp) from negative to positive values at the replication
 1005 origin and in the opposite direction from positive
 1006 to negative values at the replication terminus. This step-
 1007 like profile is characteristic of the replicon model [131]
 1008 (see Fig. 13^{TS4}, left panel). In eukaryotes, the existence
 1009 of compositional biases is unclear and most attempts to
 1010 detect the replication origins from strand compositional
 1011 asymmetry have been inconclusive. Several studies have
 1012 failed to show compositional biases related to replication,
 1013 and analysis of nucleotide substitutions in the region of
 1014 the β -globin replication origin in primates does not sup-
 1015 port the existence of mutational bias between the leading
 1016 and the lagging strands [92,147,148]. Other studies have
 1017 led to rather opposite results. For instance, strand asym-
 1018 metries associated with replication have been observed in
 1019 the subtelomeric regions of *Saccharomyces cerevisiae* chro-
 1020 mosomes, supporting the existence of replication-coupled
 1021 asymmetric mutational pressure in this organism [149].

1022 As shown in Fig. 10a for TOP1 replication origin [146],
 1023 most of the known replication origins in the human
 1024 genome correspond to rather sharp (over several kbp)
 1025 transitions from negative to positive S (S_{TA} as well as
 1026 S_{GC}) skew values that clearly emerge from the noisy back-
 1027 ground. But when examining the behavior of the skews
 1028 at larger distances from the origin, one does not observe
 1029 a step-like pattern with upward and downward jumps at
 1030 the origin and termination positions respectively as ex-
 1031 pected for the bacterial replicon model (Fig. 13, left panel).
 1032 Surprisingly, on both sides of the upward jump, the noisy
 1033 S profile decreases steadily in the 5' to 3' direction with-
 1034 out clear evidence of pronounced downward jumps. As
 1035 shown in Figs. 10b–10d, sharp upward jumps of amplitude
 1036 $\Delta S \gtrsim 15\%$, similar to the ones observed for the known
 1037 replication origins (Fig. 10a), seem to exist also at many
 1038 other locations along the human chromosomes. But the
 1039 most striking feature is the fact that in between two neigh-
 1040 boring major upward jumps, not only the noisy S profile
 1041 does not present any comparable downward sharp transi-
 1042 tion, but it displays a remarkable decreasing linear be-
 1043 havior. At chromosome scale, we thus get jagged S pro-
 1044 files that have the aspect of “factory roofs” [98,100,146].
 1045 Note that the jagged S profiles shown in Figs. 10a–10d
 1046 look somehow disordered because of the extreme variabil-
 1047 ity in the distance between two successive upward jumps,
 1048 from spacing ~ 50 – 100 kbp (~ 100 – 200 kbp for the na-
 1049 tive sequences) mainly in GC rich regions (Fig. 10d), up
 1050 to 1–2 Mbp (~ 2 – 3 Mbp for native sequences) (Fig. 10c)
 1051 in agreement with recent experimental studies [150] that
 1052 have shown that mammalian replicons are heterogeneous
 1053 in size with an average size ~ 500 kbp, the largest ones be-
 1054 ing as large as a few Mbp. But what is important to no-

1055 tice is that some of these segments between two successive
 1056 skew upward jumps are entirely intergenic (Figs. 10a, 10c),
 1057 clearly illustrating the particular profile of a strand bias re-
 1058 sulting solely from replication [98,100,146]. In most other
 1059 cases, we observe the superimposition of this replication
 1060 profile and of the step-like profiles of (+) and (–) genes
 1061 (Fig. 7), appearing as upward and downward blocks stand-
 1062 ing out from the replication pattern (Fig. 10c). Import-
 1063 antly, as illustrated in Figs. 10e, 10f, the factory-roof pat-
 1064 tern is not specific to human sequences but is also observed
 1065 in numerous regions of the mouse and dog genomes [100].
 1066 Hence, the presence of strand asymmetry in regions that
 1067 have strongly diverged during evolution further supports
 1068 the existence of compositional bias associated with replica-
 1069 tion in mammalian germ-line cells [98,100,146].

Detecting Replication Origins from the Skew WT Skeleton

1070 We have shown in Fig. 10a that experimentally deter-
 1071 mined human replication origins coincide with large-am-
 1072 plitude upward transitions in noisy skew profiles. The
 1073 corresponding ΔS ranges between 14% and 38%, owing
 1074 to possible different replication initiation efficiencies
 1075 and/or different contributions of transcriptional biases
 1076 (Sect. “Bifractality of Human DNA Strand-Asymmetry
 1077 Profiles Results from Transcription”). Along the line of the
 1078 jump detection methodology described in Sect. “Bifrac-
 1079 tality of Human DNA Strand-Asymmetry Profiles Results
 1080 from Transcription”, we have checked that upward jumps
 1081 observed in the skew S at these known replication ori-
 1082 gins correspond to maxima lines in the WT skeleton that
 1083 extend to rather large scales $a > a^* = 200$ kbp. This ob-
 1084 servation has led us to select the maxima lines that ex-
 1085 ist above $a^* = 200$ kbp, i. e. a scale which is smaller than
 1086 the typical replicon size and larger than the typical gene
 1087 size [98,100]. In this way, we not only reduce the effect of
 1088 the noise but we also reduce the contribution of the up-
 1089 ward (5' extremity) and backward (3' extremity) jumps
 1090 associated to the step-like skew pattern induced by tran-
 1091 scription only (Sect. “Bifractality of Human DNA Strand-
 1092 Asymmetry Profiles Results from Transcription”), to the
 1093 benefit of maintaining a good sensitivity to replication
 1094 induced jumps. The detected jump locations are estimated
 1095 as the positions at scale 20 kbp of the so-selected max-
 1096 ima lines. According to Eq. (11), upward (resp. down-
 1097 ward) jumps are identified by the maxima lines corre-
 1098 sponding to positive (resp. negative) values of the WT as
 1099 illustrated in Fig. 5c by the green solid (resp. dashed) max-
 1100 ima lines. When applying this methodology to the total
 1101 skew S along the repeat-masked DNA sequences of the
 1102



Fractals and Wavelets, Figure 10

S profiles along mammalian genome fragments [100,146]. **a** Fragment of human chromosome 20 including the TOP1 origin (red vertical line). **b** and **c** Human chromosome 4 and chromosome 9 fragments, respectively, with low GC content (36%). **d** Human chromosome 22 fragment with larger GC content (48%). In **a** and **b**, vertical lines correspond to selected putative origins (see Subsect. "Detecting Replication Origins from the Skew WT Skeleton"); yellow lines are linear fits of the S values between successive putative origins. **Black intergenic regions**; **red**, (+) genes; **blue**, (-) genes. Note the fully intergenic regions upstream of TOP1 in **a** and from positions 5290–6850 kbp in **c**. **e** Fragment of mouse chromosome 4 homologous to the human fragment shown in **c**. **f** Fragment of dog chromosome 5 syntenic to the human fragment shown in **c**. In **e** and **f**, genes are not represented

1104 22 human autosomal chromosomes, 2415 upward jumps
 1105 are detected and, as expected, a similar number (namely
 1106 2686) of downward jumps. In Fig. 11a are reported the
 1107 histograms of the amplitude $|\Delta S|$ of the so-identified up-
 1108 ward ($\Delta S > 0$) and downward ($\Delta S < 0$) jumps respec-
 1109 tively. These histograms no longer superimpose as previ-

ously observed at smaller scales in Fig. 8a, the former be-
 1110 ing significantly shifted to larger $|\Delta S|$ values. When plot-
 1111 ting $N(|\Delta S| > \Delta S^*)$ versus ΔS^* in Fig. 11b, we can see
 1112 that the number of large amplitude upward jumps overex-
 1113 ceeds the number of large amplitude downward jumps.
 1114 These results confirm that most of the sharp upward tran-

1115
 1116
 1117
 1118
 1119

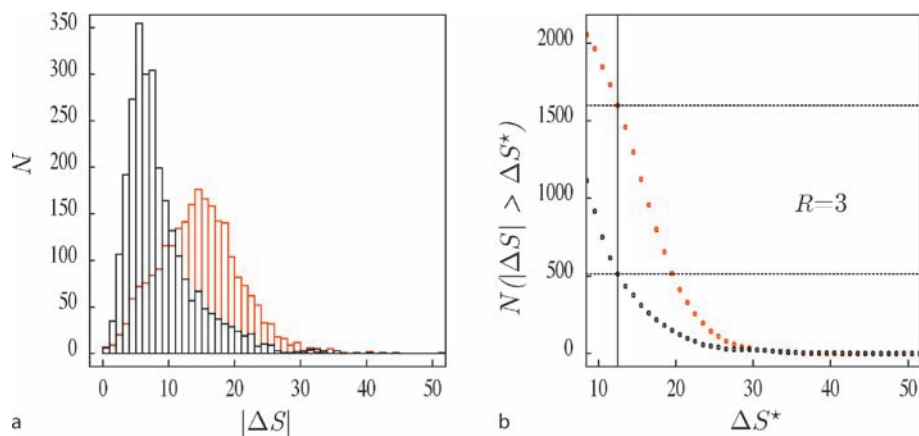
1116 sitions in the S profiles in Fig. 10 have no sharp downward
 1117 transition counterpart [98,100]. This excess likely results
 1118 from the fact that, contrasting with the prokaryote repli-
 1119 con model (Fig. 13, left panel) where downward jumps
 1120 result from precisely positioned replication terminations,
 1121 in mammals termination appears not to occur at specific
 1122 positions but to be randomly distributed. Accordingly the
 1123 small number of downward jumps with large $|\Delta S|$ is likely
 1124 to result from transcription (Fig. 5) and not from replica-
 1125 tion. These jumps are probably due to highly biased genes
 1126 that also generate a small number of large-amplitude up-
 1127 ward jumps, giving rise to false-positive candidate replica-
 1128 tion origins. In that respect, the number of large down-
 1129 ward jumps can be taken as an estimation of the number
 1130 of false positives. In a first step, we have retained as ac-
 1131 ceptable a proportion of 33% of false positives. As shown
 1132 in Fig. 11b, this value results from the selection of up-
 1133 ward and downward jumps of amplitude $|\Delta S| \geq 12.5\%$,
 1134 corresponding to a ratio of upward over downward jumps
 1135 $R = 3$. Let us notice that the value of this ratio is highly
 1136 variable along the chromosome [146] and significantly
 1137 larger than 1 for $G+C \lesssim 42\%$.

1138 In a final step, we have decided [98,100,146] to re-
 1139 tain as putative replication origins upward jumps with
 1140 $|\Delta S| \geq 12.5\%$ detected in regions with $G+C \leq 42\%$. This
 1141 selection leads to a set of 1012 candidates among which
 1142 our estimate of the proportion of true replication origins
 1143 is 79% ($R = 4.76$). In Fig. 12 is shown the mean skew pro-
 1144 file calculated in intergenic windows on both sides of the
 1145 1012 putative replication origins [100]. This mean skew
 1146 profile presents a rather sharp transition from negative to
 1147 positive values when crossing the origin position. To avoid
 1148 any bias in the skew values that could result from incom-
 1149 pletely annotated gene extremities (e. g. 5' and 3' UTRs),
 1150 we have removed 10-kbp sequences at both ends of all an-
 1151 notated transcripts. As shown in Fig. 12, the removal of
 1152 these intergenic sequences does not significantly modifies
 1153 the mean skew profile, indicating that the observed val-
 1154 ues do not result from transcription. On both sides of the
 1155 jump, we observe a linear decrease of the bias with some
 1156 flattening of the profile close to the transition point. Note
 1157 that, due to (i) the potential presence of signals implicated
 1158 in replication initiation and (ii) the possible existence of
 1159 dispersed origins [151], one might question the meaning-
 1160 fulness of this flattening that leads to a significant underes-
 1161 timate of the jump amplitude. Furthermore, according to
 1162 our detection methodology, the numerical uncertainty on
 1163 the putative origin position estimate may also contribute
 1164 to this flattening. As illustrated in Fig. 12, when extrapo-
 1165 lating the linear behavior observed at distances > 100 kbp
 1166 from the jump, one gets a skew of 5.3%, i. e. a value consis-

1167 tent with the skew measured in intergenic regions around
 1168 the six experimentally known replication origins namely
 1169 $7.0 \pm 0.5\%$. Overall, the detection of sharp upward jumps
 1170 in the skew profiles with characteristics similar to those
 1171 of experimentally determined replication origins and with
 1172 no downward counterpart further supports the existence,
 1173 in human chromosomes, of replication-associated strand
 1174 asymmetries, leading to the identification of numerous put-
 1175 ative replication origins active in germ-line cells.

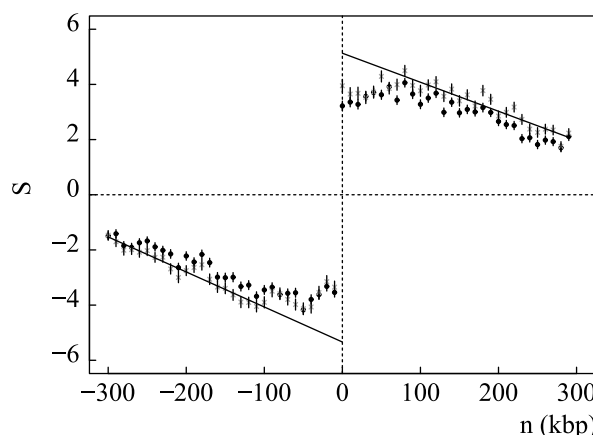
A Model of Replication in Mammalian Genomes

1176 Following the observation of jagged skew profiles similar
 1177 to factory roofs in Subsect. "Replication Induced Factory-
 1178 Roof Skew Profiles in Mammalian Genomes", and the
 1179 quantitative confirmation of the existence of such (piece-
 1180 wise linear) profiles in the neighborhood of 1012 putative
 1181 origins in Fig. 12, we have proposed, in Touchon et
 1182 al. [100] and Brodie of Brodie et al. [98], a rather crude
 1183 model for replication in the human genome that relies
 1184 on the hypothesis that the replication origins are quite
 1185 well positioned while the terminations are randomly dis-
 1186 tributed. Although some replication terminations have
 1187 been found at specific sites in *S. cerevisiae* and to some ex-
 1188 tent in *Schizosaccharomyces pombe* [152], they occur ran-
 1189 domly between active origins in *Xenopus* egg extracts [153,
 1190 154]. Our results indicate that this property can be ex-
 1191 tended to replication in human germ-line cells. As illus-
 1192 trated in Fig. 13, replication termination is likely to rely
 1193 on the existence of numerous potential termination sites
 1194 distributed along the sequence. For each termination site
 1195 (used in a small proportion of cell cycles), strand asym-
 1196 metries associated with replication will generate a step-
 1197 like skew profile with a downward jump at the position
 1198 of termination and upward jumps at the positions of the
 1199 adjacent origins (as in bacteria). Various termination po-
 1200 sitions will thus correspond to classical replicon-like skew
 1201 profiles (Fig. 13, left panel). Addition of these profiles will
 1202 generate the intermediate profile (Fig. 13, central panel).
 1203 In a simple picture, we can reasonably suppose that ter-
 1204 mination occurs with constant probability at any position
 1205 on the sequence. This behavior can, for example, result
 1206 from the binding of some termination factor at any pos-
 1207 ition between successive origins, leading to a homogeneous
 1208 distribution of termination sites during successive cell cy-
 1209 cles. The final skew profile is then a linear segment de-
 1210 creasing between successive origins (Fig. 13, right panel).
 1211 Let us point out that firing of replication origins during
 1212 time interval of the S phase [155] might result in some
 1213 flattening of the skew profile at the origins as sketched
 1214 in Fig. 13 (right panel, gray curve). In the present state,



Fractals and Wavelets, Figure 11

Statistical analysis of the sharp jumps detected in the S profiles of the 22 human autosomal chromosomes by the WT microscope at scale $a^* = 200$ kbp for repeat-masked sequences [98,100]. $|\Delta S| = |\bar{S}(3') - \bar{S}(5')|$, where the averages were computed over the two adjacent 20 kbp windows, respectively, in the 3' and 5' direction from the detected jump location. **a** Histograms $N(|\Delta S|)$ of $|\Delta S|$ values. **b** $N(|\Delta S| > \Delta S^*)$ vs. ΔS^* . In **a** and **b**, the black (resp. red) line corresponds to downward $\Delta S < 0$ (resp. upward $\Delta S > 0$) jumps. $R = 3$ corresponds to the ratio of upward over downward jumps presenting an amplitude $|\Delta S| \geq 12.5\%$ (see text)



Fractals and Wavelets, Figure 12

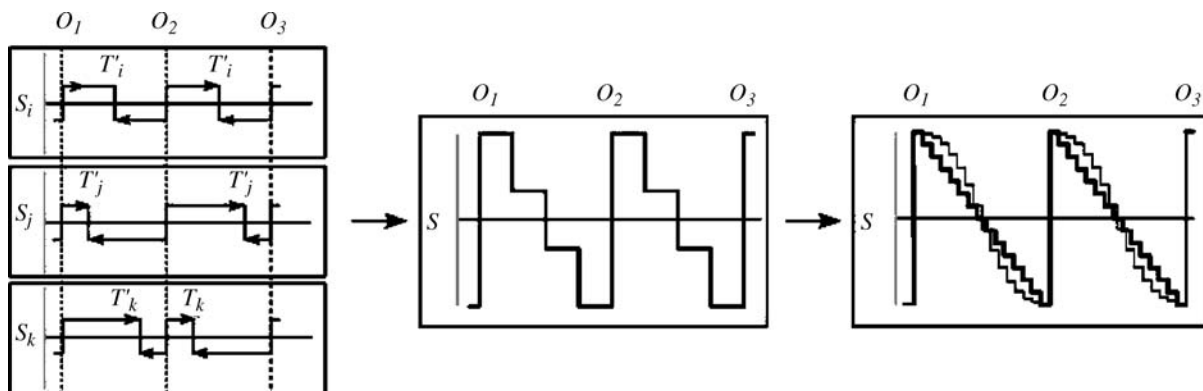
Mean skew profile of intergenic regions around putative replication origins [100]. The skew S was calculated in 1 kbp windows (Watson strand) around the position (± 300 kbp without repeats) of the 1012 detected upward jumps; 5' and 3' transcript extremities were extended by 0.5 and 2 kbp, respectively (●), or by 10 kbp at both ends (*). The abscissa represents the distance (in kbp) to the corresponding origin; the ordinate represents the skews calculated for the windows situated in intergenic regions (mean values for all discontinuities and for 10 consecutive 1 kbp window positions). The skews are given in percent (vertical bars, SEM). The lines correspond to linear fits of the values of the skew (*) for $n < -100$ kbp and $n > 100$ kbp

1216 our results [98,100,146] support the hypothesis of random
 1217 replication termination in human, and more generally in
 1218 mammalian cells (Fig. 10), but further analyzes will be nec-
 1219 essary to determine what scenario is precisely at work.

A Wavelet-Based Methodology to Disentangle Transcription- and Replication-Associated Strand Asymmetries Reveals a Remarkable Gene Organization in the Human Genome

1220
 1221
 1222
 1223

During the duplication of eukaryotic genomes that occurs 1224 during the S phase of the cell cycle, the different replica- 1225 tion origins are not all activated simultaneously [132,135, 1226 138,150,155,156]. Recent technical developments in 1227 genomic clone microarrays have led to a novel way of 1228 detecting the temporal order of DNA replication [155,156]. 1229 The arrays are used to estimate *replication timing ratios* 1230 i. e. ratios between the average amount of DNA in the S 1231 phase at a locus along the genome and the usual amount 1232 of DNA present in the $G1$ phase for that locus. These 1233 ratios should vary between 2 (throughout the S phase, the 1234 amount of DNA for the earliest replicating regions is twice 1235 the amount during $G1$ phase) and 1 (the latest replicating 1236 regions are not duplicated until the end of S phase). This 1237 approach has been successfully used to generate genome- 1238 wide maps of replication timing for *S. cerevisiae* [157], 1239 *Drosophila melanogaster* [137] and human [158]. Very 1240 recently, two new analyzes of human chromosome 6 [156] 1241 and 22 [155] have improved replication timing resolution 1242 from 1 Mbp down to ~ 100 kbp using arrays of overlap- 1243 ping tile path clones. In this section, we report on a very 1244 promising first step towards the experimental confirma- 1245 tion of the thousand putative replication origins described 1246 in Sect. “From the Detection of Relication Origins Using 1247 the Wavelet Transform Microscope to the Modeling of 1248



Fractals and Wavelets, Figure 13

Model of replication termination [98,100]. Schematic representation of the skew profiles associated with three replication origins O_1 , O_2 , and O_3 ; we suppose that these replication origins are adjacent, bidirectional origins with similar replication efficiency. The abscissa represents the sequence position; the ordinate represents the S value (arbitrary units). Upward (or downward) steps correspond to origin (or termination) positions. For convenience, the termination sites are symmetric relative to O_2 . (Left) Three different termination positions T_i , T_j , and T_k , leading to elementary skew profiles S_i , S_j , and S_k as predicted by the replicon model [146]. (Center) Superposition of these three profiles. (Right) Superposition of a large number of elementary profiles leading to the final factory-roof pattern. In the simple model, termination occurs with equal probability on both sides of the origins, leading to the linear profile (thick line). In the alternative model, replication termination is more likely to occur at lower rates close to the origins, leading to a flattening of the profile (gray line)

1249 Replication in Mammalian Genomes". The strategy will
 1250 consist in mapping them on the recent high-resolution
 1251 timing data [156] and in checking that these regions repli-
 1252 cate earlier than their surrounding [114]. But to provide
 1253 a convincing experimental test, we need as a prerequisite
 1254 to extract the contribution of the compositional skew spe-
 1255 cific to replication.

1256 Disentangling Transcription- and Replication- 1257 Associated Strand Asymmetries

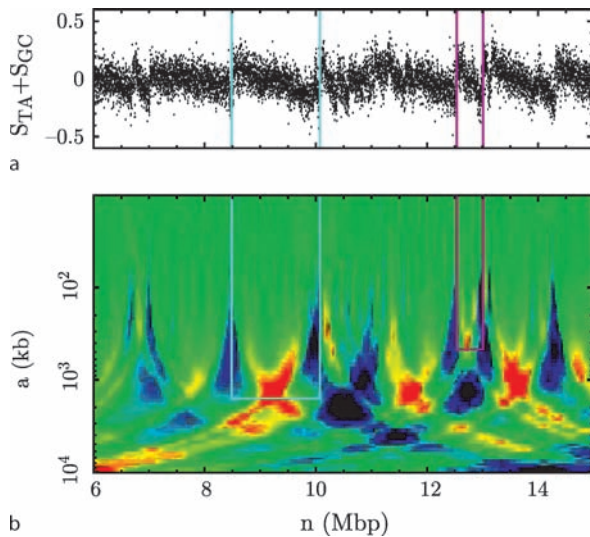
1258 The first step to detect putative replication domains
 1259 consists in developing a multi-scale pattern recognition
 1260 methodology based on the WT of the strand compo-
 1261 sitional asymmetry S using as analyzing wavelet $\phi_R(x)$
 1262 (Eq. (12)) that is adapted to perform an objective seg-
 1263 mentation of factory-roof skew profiles (Fig. 1c). As illus-
 1264 trated in Fig. 14, the space-scale location of significant max-
 1265 ima values in the 2D WT decomposition (red areas in
 1266 Fig. 14b) indicates the middle position (spatial location)
 1267 of candidate replication domains whose size is given by
 1268 the scale location. In order to avoid false positives, we then
 1269 check that there does exist a well-defined upward jump at
 1270 each domain extremity. These jumps appear in Fig. 14b as
 1271 blue cone-shape areas pointing at small scale to the jumps
 1272 positions where are located the putative replication ori-
 1273 gins. Note that because the analyzing wavelet is of zero
 1274 mean (Eq. (2)), the WT decomposition is insensitive to
 1275 (global) asymmetry offset.

But as discussed in Sect. "Bifractality of Human DNA
 Strand-Asymmetry Profiles Results from Transcription",
 the overall observed skew S also contains some contrib-
 1277 ution induced by transcription that generates step-like
 1278 blocks corresponding to (+) and (-) genes [96,97,129].
 Hence, when superimposing the replication serrated and
 1279 transcription step-like skew profiles, we get the following
 1280 theoretical skew profile in a replication domain [114]:
 1281

$$S(x') = S_R(x') + S_T(x') \\ = -2\delta \times \left(x' - \frac{1}{2} \right) + \sum_{\text{gene}} c_g \chi_g(x'), \quad (23)$$

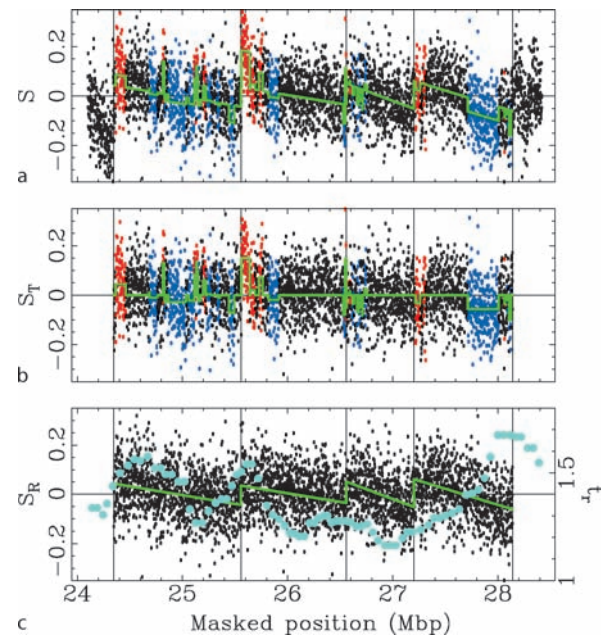
where position x' within the domain has been rescaled
 1285 between 0 and 1, $\delta > 0$ is the replication bias, χ_g is the
 1286 characteristic function for the g^{th} gene (1 when x' points
 1287 within the gene and 0 elsewhere) and c_g is its transcrip-
 1288 tional bias calculated on the Watson strand (likely to be
 1289 positive for (+) genes and negative for (-) genes). The
 1290 objective is thus to detect human replication domains by
 1291 delineating, in the noisy S profile obtained at 1 kbp resolution
 1292 (Fig. 15a), all chromosomal loci where S is well fitted by the
 1293 theoretical skew profile Eq. (23).
 1294

In order to enforce strong compatibility with the mam-
 1295 malian replicon model (Subsect. "A Model of Replication
 1296 in Mammalian Genomes"), we will only retain the do-
 1297 mains the most likely to be bordered by putative repli-
 1298 cation origins, namely those that are delimited by up-
 1299 ward jumps corresponding to a transition from a nega-
 1300



Fractals and Wavelets, Figure 14

Wavelet-based analysis of genomic sequences. **a** Skew profile S of a 9 Mbp repeat-masked fragment of human chromosome 21. **b** WT of S using φ_R (Fig. 1c); $T_{\phi_R}[S](n, a)$ is color-coded from dark-blue (min; negative values) to red (max; positive values) through green (null values). Light-blue and purple lines illustrate the detection of two replication domains of significantly different sizes. Note that in **b**, blue cone-shape areas signing upward jumps point at small scale (top) towards the putative replication origins and that the vertical positions of the WT maxima (red areas) corresponding to the two indicated replication domains match the distance between the putative replication origins (1.6 Mbp and 470 kbp respectively)



Fractals and Wavelets, Figure 15

a Skew profile S of a 4.3 Mbp repeat-masked fragment of human chromosome 6 [114]; each point corresponds to a 1 kbp window: Red, (+) genes; blue, (-) genes; black, intergenic regions (the color was defined by majority rule); the estimated skew profile (Eq. (23)) is shown in green; vertical lines correspond to the locations of 5 putative replication origins that delimit 4 adjacent domains identified by the wavelet-based methodology. **b** Transcription-associated skew S_T obtained by subtracting the estimated replication-associated profile (green lines in **c**) from the original S profile in **a**; the estimated transcription step-like profile (second term on the rhs of Eq. (23)) is shown in green. **c** Replication-associated skew S_R obtained by subtracting the estimated transcription step-like profile (green lines in **b**) from the original S profile in **a**; the estimated replication serrated profile (first term in the rhs of Eq. (23)) is shown in green; the light-blue dots correspond to high-resolution t_r data

tive S value $< -3\%$ to a positive S value $> +3\%$. Also, for each domain so-identified, we will use a least-square fitting procedure to estimate the replication bias δ , and each of the gene transcription bias c_g . The resulting χ^2 value will then be used to select the candidate domains where the noisy S profile is well described by Eq. (23). As illustrated in Fig. 15 for a fragment of human chromosome 6 that contains 4 adjacent replication domains (Fig. 15a), this method provides a very efficient way of disentangling the step-like transcription skew component (Fig. 15b) from the serrated component induced by replication (Fig. 15c). Applying this procedure to the 22 human autosomes, we delineated 678 replication domains of mean length $\langle L \rangle = 1.2 \pm 0.6$ Mbp, spanning 28.3% of the genome and predicted 1060 replication origins.

1316 DNA Replication Timing Data Corroborate *in silico* 1317 Human Replication Origin Predictions

1318 Chromosome 22 being rather atypical in gene and GC
1319 contents, we mainly report here on the correlation analy-

sis [114] between nucleotide compositional skew and timing data for chromosome 6 which is more representative of the whole human genome. Note that timing data for clones completely included in another clone have been removed after checking for timing ratio value consistency leaving 1648 data points. The timing ratio value at each point has been chosen as the median over the 4 closest data points to remove noisy fluctuations resulting from clone heterogeneity (clone length 100 ± 51 kbp and distance between successive clone mid-points 104 ± 89 kbp), so that the spatial resolution is rather inhomogeneous ~ 300 kbp. Note that using asynchronous cells also results in some smoothing of the data, possibly masking local maxima.

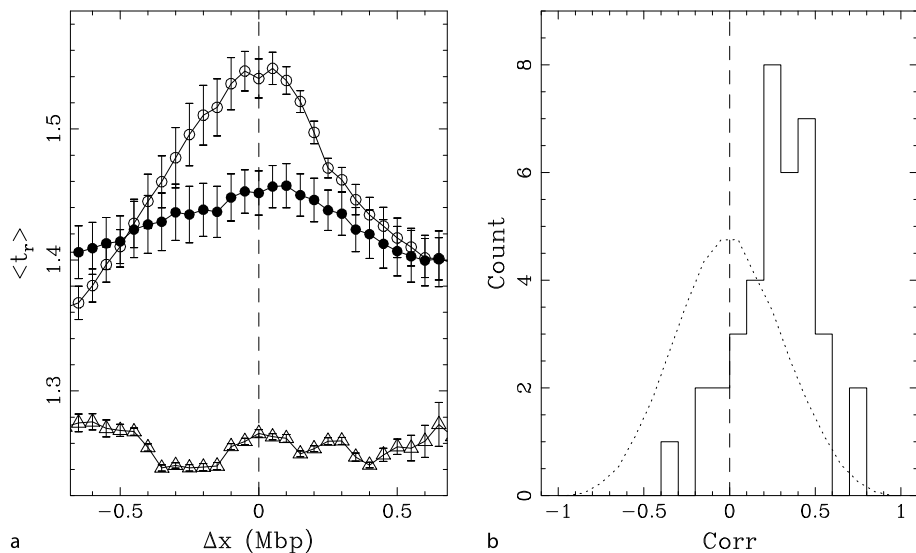
1320
1321
1322
1323
1324
1325
1326
1327
1328
1329
1330
1331
1332

1333 Our wavelet-based methodology has identified 54
 1334 replication domains in human chromosome 6 [114]; these
 1335 domains are bordered by 83 putative replication origins
 1336 among which 25 are common to two adjacent domains.
 1337 Four of these contiguous domains are shown in Fig. 15.
 1338 In Fig. 15c, on top of the replication skew profile S_R , are
 1339 reported for comparison the high-resolution timing ratio
 1340 t_r data from [156]. The histogram of t_r values obtained
 1341 at the 83 putative origin locations displays a maximum
 1342 at $t_r \simeq \langle t_r \rangle \simeq 1.5$ (data not shown) and confirms what is
 1343 observed in Fig. 15c, namely that a majority of the pre-
 1344 dicted origins are rather early replicating with $t_r \gtrsim 1.4$.
 1345 This contrasts with the rather low t_r ($\simeq 1.2$) values ob-
 1346 served in domain central regions (Fig. 15c). But there is
 1347 an even more striking feature in the replication timing
 1348 profile in Fig. 15c: 4 among the 5 predicted origins cor-
 1349 respond, relatively to the experimental resolution, to lo-
 1350 cal maxima of the t_r profile. As shown in Fig. 16a, the
 1351 average t_r profile around the 83 putative replication ori-
 1352 gins decreases regularly on both sides of the origins over
 1353 a few (4–6) hundreds kbp confirming statistically that do-
 1354 main borders replicate earlier than their left and right sur-
 1355 roundings which is consistent with these regions being
 1356 true replication origins mostly active early in S phase. In
 1357 fact, when averaging over the top 20 origins with a well-de-
 1358 fined local maximum in the t_r profile, $\langle t_r \rangle$ displays a faster
 1359 decrease on both sides of the origin and a higher max-
 1360 imum value ~ 1.55 corresponding to the earliest repli-
 1361 cating origins. On the opposite, when averaging t_r pro-
 1362 files over the top 10 late replicating origins, we get, as ex-
 1363 pected, a rather flat mean profile ($t_r \sim 1.2$) (Fig. 16a). In-
 1364 terestingly, these origins are located in rather wide regions
 1365 of very low GC content ($\lesssim 34\%$, not shown) correlat-
 1366 ing with chromosomal G banding patterns predominantly
 1367 composed of GC-poor isochores [159,160]. This illustrates
 1368 how the statistical contribution of rather flat profiles ob-
 1369 served around late replicating origins may significantly af-
 1370 fect the overall mean t_r profile. Individual inspection of
 1371 the 38 replication domains with $L \geq 1$ Mbp shows that, in
 1372 those domains that are bordered by early replicating ori-
 1373 gins ($t_r \gtrsim 1.4 - 1.5$), the replication timing ratio t_r and the
 1374 absolute value of the replication skew $|S_R|$ turn out to be
 1375 strongly correlated. This is quantified in Fig. 16b by the
 1376 histogram of the Pearson's correlation coefficient values
 1377 that is clearly shifted towards positive values with a max-
 1378 imum at ~ 0.4 . Altogether the results of this comparative
 1379 analysis provide the first experimental verification of *in*
 1380 *silico* replication origins predictions: The detected puta-
 1381 tive replication domains are bordered by replication ori-
 1382 gins mostly active in the early S phase, whereas the central
 1383 regions replicate more likely in late S phase.

Gene Organization in the Detected Replication Domains

1384
 1385
 1386 Most of the 1060 putative replication origins that bor-
 1387 der the detected replication domains are intergenic (77%)
 1388 and are located near to a gene promoter more often than
 1389 would be expected by chance (data not shown) [101]. The
 1390 replication domains contain approximately equal num-
 1391 bers of genes oriented in each direction (1511 (+) genes
 1392 and 1507 (–) genes). Gene distributions in the 5' halves
 1393 of domains contain more (+) genes than (–) genes, re-
 1394 gardless of the total number of genes located in the half-
 1395 domains (Fig. 17b). Symmetrically, the 3' halves contain
 1396 more (–) genes than (+) genes (Fig. 17b). 32.7% of half-
 1397 domains contain one gene, and 50.9% contain more than
 1398 one gene. For convenience, (+) genes in the 5' halves
 1399 and (–) genes in the 3' halves are defined as R+ genes
 1400 (Fig. 17a): Their transcription is, in most cases, oriented
 1401 in the same direction as the putative replication fork pro-
 1402 gression (genes transcribed in the opposite direction are
 1403 defined as R– genes). The 678 replication domains contain
 1404 significantly more R+ genes (2041) than R– genes (977).
 1405 Within 50 kbp of putative replication origins, the mean
 1406 density of R+ genes is 8.2 times greater than that of R–
 1407 genes. This asymmetry weakens progressively with the
 1408 distance from the putative origins, up to ~ 250 kbp (Fig. 17b).
 1409 A similar asymmetric pattern is observed when the do-
 1410 mains containing duplicated genes are eliminated from
 1411 the analysis, whereas control domains obtained after ran-
 1412 domization of domain positions present similar R+ and
 1413 R– gene density distributions (Supplementary in [101]).
 1414 The mean length of the R+ genes near the putative ori-
 1415 gins is significantly greater (~ 160 kbp) than that of the
 1416 R– genes (~ 50 kbp), however both tend towards similar
 1417 values (~ 70 kbp) at the center of the domain (Fig. 17c).
 1418 Within 50 kbp of the putative origins, the ratio between
 1419 the numbers of base pairs transcribed in the R+ and R– di-
 1420 rections is 23.7; this ratio falls to ~ 1 at the domain centers
 1421 (Fig. 17d). In Fig. 17e are reported the results of the anal-
 1422 ysis of the breadth of expression, N_t (number of tissues in
 1423 which a gene is expressed) of genes located within the de-
 1424 tected domains [101]. As measured by EST data (similar
 1425 results are obtained by SAGE or microarray data [101]),
 1426 N_t is found to decrease significantly from the extremities
 1427 to the center in a symmetrical manner in the 5' and 3' half-
 1428 domains (Fig. 17e). Thus, genes located near the putative
 1429 replication origins tend to be widely expressed whereas
 1430 those located far from them are mostly tissue-specific.

1431 To summarize, the results reported in this section pro-
 1432 vide the first demonstration of quantitative relationships
 1433 in the human genome between gene expression, orienta-



Fractals and Wavelets, Figure 16

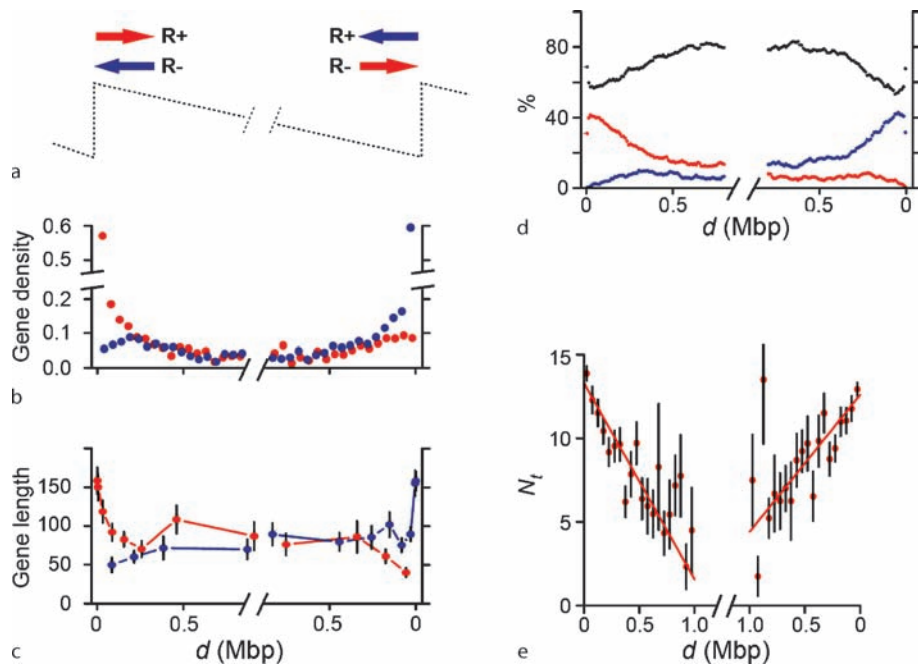
a Average replication timing ratio (\pm SEM) determined around the 83 putative replication origins (●), 20 origins with well-defined local maxima (○) and 10 late replicating origins (Δ). Δx is the native distance to the origins in Mbp units [114]. **b** Histogram of Pearson's correlation coefficient values between t_r and the absolute value of S_R over the 38 predicted domains of length $L \geq 1$ Mbp. The dotted line corresponds to the expected histogram computed with the correlation coefficients between t_r and $|S|$ profiles over independent windows randomly positioned along chromosome 6 and with the same length distribution as the 38 detected domains

1434 tation and distance from putative replication origins [101].
 1435 A possible key to the understanding of this complex archi-
 1436 tecture is the coordination between replication and trans-
 1437 cription [101]. The putative replication origins would
 1438 mostly be active early in the S phase in most tissues. Their
 1439 activity could result from particular genomic context in-
 1440 volving transcription factor binding sites and/or from the
 1441 transcription of their neighboring housekeeping genes.
 1442 This activity could also be associated with an open chro-
 1443 matin structure, permissive to early replication and gene
 1444 expression in most tissues [161,162,163,164]. This open
 1445 conformation could extend along the first gene, possi-
 1446 bly promoting the expression of further genes. This ef-
 1447 fect would progressively weaken with the distance from
 1448 the putative replication origin, leading to the observed de-
 1449 crease in expression breadth. This model is consistent with
 1450 a number of data showing that in metazoans, ORC and
 1451 RNA polymerase II colocalize at transcriptional promoter
 1452 regions [165], and that replication origins are determined
 1453 by epigenetic information such as transcription factor
 1454 binding sites and/or transcription [166,167,168,169]. It is
 1455 also consistent with studies in *Drosophila* and humans that
 1456 report correlation between early replication timing and
 1457 increased probability of expression [137,155,156,165,170].
 1458 Furthermore, near the putative origins bordering the repli-
 1459 cation domains, transcription is preferentially oriented in
 1460 the same direction as replication fork progression. This co-

1461 orientation is likely to reduce head-on collisions between
 1462 the replication and transcription machineries, which may
 1463 induce deleterious recombination events either directly or
 1464 via stalling of the replication fork [171,172]. In bacteria,
 1465 co-orientation of transcription and replication has been
 1466 observed for essential genes, and has been associated with
 1467 a reduction in head-on collisions between DNA and RNA
 1468 polymerases [173]. It is noteworthy that in human replica-
 1469 tion domains such co-orientation usually occurs in widely-
 1470 expressed genes located near putative replication origins.
 1471 Near domain centers, head-on collisions may occur in 50%
 1472 of replication cycles, regardless of the transcription ori-
 1473 entation, since there is no preferential orientation of the
 1474 replication fork progression in these regions. However, in
 1475 most cell types, there should be few head-on collisions due
 1476 to the low density and expression breadth of the corre-
 1477 sponding genes. Selective pressure to reduce head-on col-
 1478 lisions may thus have contributed to the simultaneous and
 1479 coordinated organization of gene orientation and expres-
 1480 sion breadth along the detected replication domains [101].

Future Directions

1481 From a statistical multifractal analysis of nucleotide strand
 1482 asymmetries in mammalian genomes, we have revealed
 1483 the existence of jumps in the noisy skew profiles result-
 1484 ing from asymmetries intrinsic to the transcription and



Fractals and Wavelets, Figure 17

Analysis of the genes located in the identified replication domains [101]. a Arrows indicate the R+ orientation, i. e. the same orientation as the most frequent direction of putative replication fork progression; R- orientation (opposed direction); red, (+) genes; blue, (-) genes. b Gene density. The density is defined as the number of 5' ends (for (+) genes) or of 3' ends (for (-) genes) in 50-kbp adjacent windows, divided by the number of corresponding domains. In abscissa, the distance, d , in Mbp, to the closest domain extremity. c Mean gene length. Genes are ranked by their distance, d , from the closest domain extremity, grouped by sets of 150 genes, and the mean length (kbp) is computed for each set. d Relative number of base pairs transcribed in the + direction (red), - direction (blue) and non-transcribed (black) determined in 10-kbp adjacent sequence windows. e Mean expression breadth using EST data [101]

replication processes [98,100]. This discovery has led us to extend our 1D WTMM methodology to an adapted multi-scale pattern recognition strategy in order to detect putative replication domains bordered by replication origins [101,114]. The results reported in this manuscript show that directly from the DNA sequence, we have been able to reveal the existence in the human genome (and very likely in all mammalian genomes), of regions bordered by early replicating origins in which gene position, orientation and expression breadth present a high level of organization, possibly mediated by the chromatin structure.

These results open new perspectives in DNA sequence analysis, chromatin modeling as well as in experiment. From a bioinformatic and modeling point of view, we plan to study the lexical and structural characteristics of our set of putative origins. In particular we will search for conserved sequence motifs in these replication initiation zones. Using a sequence-dependent model of DNA-histones interactions, we will develop physical studies of nucleosome formation and diffusion along the DNA fiber around the putative replication origins. These bioinfor-

matic and physical studies, performed for the first time on a large number of replication origins, should shed light on the processes at work during the recognition of the replication initiation zone by the replication machinery. From an experimental point of view, our study raises new opportunities for future experiments. The first one concerns the experimental validation of the predicted replication origins (e. g. by molecular combing of DNA molecules [174]), which will allow us to determine precisely the existence of replication origins in given genome regions. Large scale study of all candidate origins is in current progress in the laboratory of O. Hyrien (École Normale Supérieure, Paris). The second experimental project consists in using Atomic Force Microscopy (AFM) [175] and Surface Plasmon Resonance Microscopy (SPRM) [176] to visualize and study the structural and mechanical properties of the DNA double helix, the nucleosomal string and the 30 nm chromatin fiber around the predicted replication origins. This work is in current progress in the experimental group of F. Argoul and C. Moskalenko at the Laboratoire Joliot-Curie (ENS, Lyon) [83]. Finally the third experimental

1486 1507
1487 1508
1488 1509
1489 1510
1490 1511
1491 1512
1492 1513
1493 1514
1494 1515
1495 1516
1496 1517
1497 1518
1498 1519
1499 1520
1500 1521
1501 1522
1502 1523
1503 1524
1504 1525
1505 1526
1506 1527

1528 perspective concerns in situ studies of replication origins.
 1529 Using fluorescence techniques (FISH chromosome painting [177]), we plan to study the distributions and dynamics
 1530 of origins in the cell nucleus, as well as chromosome domains potentially associated with territories and their
 1531 possible relation to nuclear matrix attachment sites. This study is likely to provide evidence of chromatin rosette
 1532 patterns as suggested in [146]. This study is under progress in the molecular biology experimental group of F. Monge-
 1533 lard at the Laboratoire Joliot-Curie.
 1534

1538 Acknowledgments

1539 We thank O. Hyrien, F. Mongelard and C. Moskalenko
 1540 for interesting discussions. This work was supported by
 1541 the Action Concertée Incitative Informatique, Mathéma-
 1542 tiques, Physique en Biologie Moléculaire 2004 under the
 1543 project “ReplicOr”, the Agence Nationale de la Recherche
 1544 under the project “HUGOREP” and the program “Emer-
 1545 gence” of the Conseil Régional Rhônes-Alpes and by the
 1546 Programme d’Actions Intégrées Tournesol.

1547 Bibliography

1548 Primary Literature

1. Goupillaud P, Grossmann A, Morlet J (1984) Cycle-octave and related transforms in seismic signal analysis. *Geoexploration* 23:85–102
2. Grossmann A, Morlet J (1984) Decomposition of Hardy functions into square integrable wavelets of constant shape. *SIAM J Math Anal* 15:723–736
3. Arneodo A, Argoul F, Bacry E, Elezgaray J, Freysz E, Grasseau G, Muzy J-F, Pouliquen B (1992) Wavelet transform of fractals. In: Meyer Y (ed) *Wavelets and applications*. Springer, Berlin, pp 286–352
4. Arneodo A, Argoul F, Elezgaray J, Grasseau G (1989) Wavelet transform analysis of fractals: Application to nonequilibrium phase transitions. In: Turchetti G (ed) *Nonlinear dynamics*. World Scientific, Singapore, pp 130–180
5. Arneodo A, Grasseau G, Holschneider M (1988) Wavelet transform of multifractals. *Phys Rev Lett* 61:2281–2284
6. Holschneider M (1988) On the wavelet transform of fractal objects. *J Stat Phys* 50:963–993
7. Holschneider M, Tchamitchian P (1990) Régularité locale de la fonction non-différentiable de Riemann. In: Lemarié PG (ed) *Les ondelettes en 1989*. Springer, Berlin, pp 102–124
8. Jaffard S (1989) Hölder exponents at given points and wavelet coefficients. *C R Acad Sci Paris Sér. I* 308:79–81
9. Jaffard S (1991) Pointwise smoothness, two-microlocalization and wavelet coefficients. *Publ Mat* 35:155–168
10. Mallat S, Hwang W (1992) Singularity detection and processing with wavelets. *IEEE Trans Info Theory* 38:617–643
11. Mallat S, Zhong S (1992) Characterization of signals from multiscale edges. *IEEE Trans Patt Recog Mach Intell* 14:710–732
12. Arneodo A, Bacry E, Muzy J-F (1995) The thermodynamics of fractals revisited with wavelets. *Physica A* 213:232–275
13. Bacry E, Muzy J-F, Arneodo A (1993) Singularity spectrum of fractal signals from wavelet analysis: Exact results. *J Stat Phys* 70:635–674
14. Muzy J-F, Bacry E, Arneodo A (1991) Wavelets and multifractal formalism for singular signals: Application to turbulence data. *Phys Rev Lett* 67:3515–3518
15. Muzy J-F, Bacry E, Arneodo A (1993) Multifractal formalism for fractal signals: The structure-function approach versus the wavelet-transform modulus-maxima method. *Phys Rev E* 47:875–884
16. Muzy J-F, Bacry E, Arneodo A (1994) The multifractal formalism revisited with wavelets. *Int J Bifurc Chaos* 4:245–302
17. Jaffard S (1997) Multifractal formalism for functions part I: Results valid for all functions. *SIAM J Math Anal* 28:944–970
18. Jaffard S (1997) Multifractal formalism for functions part II: Self-similar functions. *SIAM J Math Anal* 28:971–998
19. Hentschel HGE (1994) Stochastic multifractality and universal scaling distributions. *Phys Rev E* 50:243–261
20. Arneodo A, Audit B, Decoster N, Muzy J-F, Vaillant C (2002) Wavelet based multifractal formalism: Application to DNA sequences, satellite images of the cloud structure and stock market data. In: Bunde A, Kropp J, Schellnhuber HJ (eds) *The science of disasters: Climate disruptions, heart attacks, and market crashes*. Springer, Berlin, pp 26–102
21. Arneodo A, Manneville S, Muzy J-F (1998) Towards log-normal statistics in high reynolds number turbulence. *Eur Phys J B* 1:129–140
22. Arneodo A, Manneville S, Muzy J-F, Roux SG (1999) Revealing a lognormal cascading process in turbulent velocity statistics with wavelet analysis. *Phil Trans R Soc Lond A* 357:2415–2438
23. Delour J, Muzy J-F, Arneodo A (2001) Intermittency of 1D velocity spatial profiles in turbulence: A magnitude cumulant analysis. *Eur Phys J B* 23:243–248
24. Roux S, Muzy J-F, Arneodo A (1999) Detecting vorticity filaments using wavelet analysis: About the statistical contribution of vorticity filaments to intermittency in swirling turbulent flows. *Eur Phys J B* 8:301–322
25. Venugopal V, Roux SG, Foufoula-Georgiou E, Arneodo A (2006) Revisiting multifractality of high-resolution temporal rainfall using a wavelet-based formalism. *Water Resour Res* 42:W06D14 [TS5]
26. Venugopal V, Roux SG, Foufoula-Georgiou E, Arneodo A (2006) Scaling behavior of high resolution temporal rainfall: New insights from a wavelet-based cumulant analysis. *Phys Lett A* 348:335–345
27. Arneodo A, d’Aubenton-Carafa Y, Bacry E, Graves PV, Muzy J-F, Thermes C (1996) Wavelet based fractal analysis of DNA sequences. *Physica D* 96:291–320
28. Arneodo A, Bacry E, Graves PV, Muzy J-F (1995) Characterizing long-range correlations in DNA sequences from wavelet analysis. *Phys Rev Lett* 74:3293–3296
29. Audit B, Thermes C, Vaillant C, d’Aubenton Carafa Y, Muzy J-F, Arneodo A (2001) Long-range correlations in genomic DNA: A signature of the nucleosomal structure. *Phys Rev Lett* 86:2471–2474
30. Audit B, Vaillant C, Arneodo A, d’Aubenton Carafa Y, Thermes C (2002) Long-range correlations between DNA bending sites: Relation to the structure and dynamics of nucleosomes. *J Mol Biol* 316:903–918
31. Arneodo A, Muzy J-F, Sornette D (1998) “Direct” causal cascade in the stock market. *Eur Phys J B* 2:277–282

TS5 Please check page range.

1641 32. Muzy J-F, Sornette D, Delour J, Arneodo A (2001) Multifractal returns and hierarchical portfolio theory. *Quant Finance* 1:131–148 1702

1642 33. Ivanov PC, Amaral LA, Goldberger AL, Havlin S, Rosenblum 1703

1643 MG, Struzik ZR, Stanley HE (1999) Multifractality in human 1704

1644 heartbeat dynamics. *Nature* 399:461–465 1705

1645 34. Ivanov PC, Rosenblum MG, Peng CK, Mietus J, Havlin S, Stanley 1706

1646 HE, Goldberger AL (1996) Scaling behavior of heartbeat 1707

1647 intervals obtained by wavelet-based time-series analysis. *Nature* 383:323–327 1708

1648 35. Arneodo A, Argoul F, Bacry E, Muzy J-F, Tabard M (1992) 1709

1649 Golden mean arithmetic in the fractal branching of diffusion- 1710

1650 limited aggregates. *Phys Rev Lett* 68:3456–3459 1711

1651 36. Arneodo A, Argoul F, Muzy J-F, Tabard M (1992) Structural 1712

1652 5-fold symmetry in the fractal morphology of diffusion-limited 1713

1653 aggregates. *Physica A* 188:217–242 1714

1654 37. Arneodo A, Argoul F, Muzy J-F, Tabard M (1992) Uncovering 1715

1655 Fibonacci sequences in the fractal morphology of diffusion-limited 1716

1656 aggregates. *Phys Lett A* 171:31–36 1717

1657 38. Kuhn A, Argoul F, Muzy J-F, Arneodo A (1994) Structural-analysis 1718

1658 of electroless deposits in the diffusion-limited regime. *Phys Rev Lett* 73:2998–3001 1719

1659 39. Arneodo A, Decoster N, Roux SG (2000) A wavelet-based 1720

1660 method for multifractal image analysis, I. Methodology and 1721

1661 test applications on isotropic and anisotropic random rough 1722

1662 surfaces. *Eur Phys J B* 15:567–600 1723

1663 40. Arrault J, Arneodo A, Davis A, Marshak A (1997) Wavelet 1724

1664 based multifractal analysis of rough surfaces: Application to 1725

1665 cloud models and satellite data. *Phys Rev Lett* 79:75–78 1726

1666 41. Decoster N, Roux SG, Arneodo A (2000) A wavelet-based 1727

1667 method for multifractal image analysis, II. Applications to 1728

1668 synthetic multifractal rough surfaces. *Eur Phys J B* 15:739–764 1729

1669 42. Arneodo A, Decoster N, Roux SG (1999) Intermittency, 1730

1670 log-normal statistics, and multifractal cascade process in high- 1731

1671 resolution satellite images of cloud structure. *Phys Rev Lett* 83:1255–1258 1732

1672 43. Roux SG, Arneodo A, Decoster N (2000) A wavelet-based 1733

1673 method for multifractal image analysis, III. Applications to 1734

1674 high-resolution satellite images of cloud structure. *Eur Phys 1735*

1675 J B 15:75–786 1736

1676 44. Khalil A, Joncas G, Nekka F, Kestener P, Arneodo A (2006) 1737

1677 Morphological analysis of H_f features, II. Wavelet-based multifractal 1738

1678 formalism. *Astrophys J Suppl Ser* 165:512–550 1739

1679 45. Kestener P, Lina J-M, Saint-Jean P, Arneodo A (2001) Wavelet- 1740

1680 based multifractal formalism to assist in diagnosis in digitized 1741

1681 mammograms. *Image Anal Stereol* 20:169–174 1742

1682 46. Arneodo A, Decoster N, Kestener P, Roux SG (2003) A wavelet- 1743

1683 based method for multifractal image analysis: From theoretical 1744

1684 concepts to experimental applications. *Adv Imaging Electr Phys* 126:1–92 1745

1685 47. Kestener P, Arneodo A (2003) Three-dimensional wavelet- 1746

1686 based multifractal method: The need for revisiting the 1747

1687 multifractal description of turbulence dissipation data. *Phys Rev 1748*

1688 Lett

1689 91:194501 **TS5** 1749

1690 48. Meneveau C, Sreenivasan KR (1991) The multifractal nature 1750

1691 of turbulent energy-dissipation. *J Fluid Mech* 224:429–484 1751

1692 49. Kestener P, Arneodo A (2004) Generalizing the wavelet-based 1752

1693 multifractal formalism to random vector fields: Application 1753

1694 to three-dimensional turbulence velocity and vorticity data. 1754

1695 *Phys Rev Lett* 93:044501 **TS5** 1755

1696 50. Kestener P, Arneodo A (2007) A multifractal formalism for 1756

1697 1700 vector-valued random fields based on wavelet analysis: Application 1701

1698 to turbulent velocity and vorticity 3D numerical data. *Stoch Environ Res Risk Assess*. **TS6** doi:10.1007/s00477-007-0121-6 1702

1701 51. Li WT, Marr TG, Kaneko K (1994) Understanding long-range 1703

1702 correlations in DNA-sequences. *Physica D* 75:392–416 1704

1703 52. Stanley HE, Buldyrev SV, Goldberger AL, Havlin S, Ossadnik 1705

1704 SM, Peng C-K, Simons M (1993) Fractal landscapes in biological 1706

1705 systems. *Fractals* 1:283–301 1707

1706 53. Li W (1990) Mutual information functions versus correlation- 1708

1707 functions. *J Stat Phys* 60:823–837 1709

1708 54. Li W (1992) Generating non trivial long-range correlations 1710

1709 and $1/f$ spectra by replication and mutation. *Int J Bifurc Chaos* 2:137–154 1711

1710 55. Azbel' MY (1995) Universality in a DNA statistical structure. 1712

1711 *Phys Rev Lett* 75:168–171 1713

1712 56. Herzel H, Große I (1995) Measuring correlations in symbol 1714

1713 sequences. *Physica A* 216:518–542 1715

1714 57. Voss RF (1992) Evolution of long-range fractal correlations 1716

1715 and $1/f$ noise in DNA base sequences. *Phys Rev Lett* 68: 1717

1716 3805–3808 1718

1717 58. Voss RF (1994) Long-range fractal correlations in DNA introns 1719

1718 and exons. *Fractals* 2:1–6 1720

1719 59. Peng C-K, Buldyrev SV, Goldberger AL, Havlin S, Sciortino F, 1721

1720 Simons M, Stanley HE (1992) Long-range correlations in nucleotide 1722

1721 sequences. *Nature* 356:168–170 1723

1722 60. Havlin S, Buldyrev SV, Goldberger AL, Mantegna RN, Peng 1724

1723 C-K, Simons M, Stanley HE (1995) Statistical and linguistic features 1725

1724 of DNA sequences. *Fractals* 3:269–284 1726

1725 61. Mantegna RN, Buldyrev SV, Goldberger AL, Havlin S, Peng 1727

1726 C-K, Simons M, Stanley HE (1995) Systematic analysis of coding 1728

1727 and noncoding DNA sequences using methods of statistical 1729

1728 linguistics. *Phys Rev E* 52:2939–2950 1730

1729 62. Herzel H, Ebeling W, Schmitt A (1994) Entropies of biosequences: 1731

1730 The role of repeats. *Phys Rev E* 50:5061–5071 1731

1731 63. Li W (1997) The measure of compositional heterogeneity in 1732

1732 DNA sequences is related to measures of complexity. *Complexity* 3:33–37 1733

1733 64. Borštník B, Pumpernik D, Lukman D (1993) Analysis of apparent 1734

1734 $1/f^\alpha$ spectrum in DNA sequences. *Europhys Lett* 23:389–394 1735

1735 65. Chatzidimitriou-Dreismann CA, Larhammar D (1993) Long- 1736

1736 range correlations in DNA. *Nature* 361:212–213 1737

1737 66. Nee S (1992) Uncorrelated DNA walks. *Nature* 357:450 1738

1738 67. Viswanathan GM, Buldyrev SV, Havlin S, Stanley HE (1998) 1739

1739 Long-range correlation measures for quantifying patchiness: 1740

1740 Deviations from uniform power-law scaling in genomic DNA. 1741

1741 *Physica A* 249:581–586 1742

1742 68. Buldyrev SV, Goldberger AL, Havlin S, Mantegna RN, Matsa 1743

1743 ME, Peng C-K, Simons M, Stanley HE (1995) Long-range correlation 1744

1744 properties of coding and noncoding DNA sequences: GenBank 1745

1745 analysis. *Phys Rev E* 51:5084–5091 1746

1746 69. Berthelsen CL, Glazier JA, Raghavachari S (1994) Effective 1747

1747 multifractal spectrum of a random walk. *Phys Rev E* 49: 1748

1748 1860–1864 1749

1749 70. Li W (1997) The study of correlation structures of DNA 1750

1750 sequences: A critical review. *Comput Chem* 21:257–271 1751

1751 71. Peng C-K, Buldyrev SV, Goldberger AL, Havlin S, Simons M, 1752

1752 Stanley HE (1993) Finite-size effects on long-range correlations: 1753

1753 Implications for analyzing DNA sequences. *Phys Rev E* 47:3730–3733 1754

1754 1761

TS6 Please provide volume and page range.

1763 72. Bernardi G (2000) Isochores and the evolutionary genomics 1824
1764 of vertebrates. *Gene* 241:3–17 1825

1765 73. Gardiner K (1996) Base composition and gene distribution: 1826
1766 Critical patterns in mammalian genome organization. *Trends* 1827
1767 *Genet* 12:519–524 1828

1768 74. Li W, Stolovitzky G, Bernaola-Galván P, Oliver JL (1998) 1829
1769 Compositional heterogeneity within, and uniformity between, 1830
1770 DNA sequences of yeast chromosomes. *Genome Res* 8: 1831
1771 916–928 1832

1772 75. Karlin S, Brendel V (1993) Patchiness and correlations in 1833
1773 DNA sequences. *Science* 259:677–680 1834

1774 76. Larhammar D, Chatzidimitriou-Dreismann CA (1993) 1835
1775 Biological origins of long-range correlations and compositional 1836
1776 variations in DNA. *Nucleic Acids Res* 21:5167–5170 1837

1777 77. Peng C-K, Buldyrev SV, Havlin S, Simons M, Stanley HE, Gold- 1838
1778 berger AL (1994) Mosaic organization of DNA nucleotides. 1839
1779 *Phys Rev E* 49:1685–1689 1840

1780 78. Arneodo A, d'Aubenton-Carafa Y, Audit B, Bacry E, Muzy 1841
1781 J-F, Thermes C (1998) Nucleotide composition effects on the 1842
1782 long-range correlations in human genes. *Eur Phys J B* 1: 1843
1783 259–263 1844

1784 79. Vaillant C, Audit B, Arneodo A (2005) Thermodynamics of 1845
1785 DNA loops with long-range correlated structural disorder. 1846
1786 *Phys Rev Lett* 95:068101 **TS5** 1847

1787 80. Vaillant C, Audit B, Thermes C, Arneodo A (2006) Formation 1848
1788 and positioning of nucleosomes: effect of sequence-depen- 1849
1789 dent long-range correlated structural disorder. *Eur Phys J E* 1850
1790 19:263–277 1851

1791 81. Yuan G-C, Liu Y-J, Dion MF, Slack MD, Wu LF, Altschuler SJ, 1852
1792 Rando OJ (2005) Genome-scale identification of nucleosome 1853
1793 positions in *S. cerevisiae*. *Science* 309:626–630 1854

1794 82. Vaillant C, Audit B, Arneodo A (2007) Experiments confirm the 1855
1795 influence of genome long-range correlations on nucleosome 1856
1796 positioning. *Phys Rev Lett* (submitted) **TS7** 1857

1797 83. Moukhtar J, Fontaine E, Faivre-Moskalenko C, Arneodo A 1858
1798 (2007) Probing persistence in DNA curvature properties with 1859
1799 atomic force microscopy. *Phys Rev Lett* 98:178101 **TS5** 1860

1800 84. Chargaff E (1951) Structure and function of nucleic acids as 1861
1801 cell constituents. *Fed Proc* 10:654–659 1862

1802 85. Rudner R, Karkas JD, Chargaff E (1968) Separation of *B. subtilis* 1863
1803 DNA into complementary strands, 3. Direct analysis. *Proc Natl 1864
1804 Acad Sci USA* 60:921–922 1865

1805 86. Fickett JW, Torney DC, Wolf DR (1992) Base compositional 1866
1806 structure of genomes. *Genomics* 13:1056–1064 1867

1807 87. Lobry JR (1995) Properties of a general model of DNA evolution 1868
1808 under no-strand-bias conditions. *J Mol Evol* 40:326–330 1869

1809 88. Beletskii A, Grigoriev A, Joyce S, Bhagwat AS (2000) 1870
1810 Mutations induced by bacteriophage T7 RNA polymerase and their 1871
1811 effects on the composition of the T7 genome. *J Mol Biol* 1872
1812 300:1057–1065 1873

1813 89. Francino MP, Ochman H (2001) Deamination as the basis of 1874
1814 strand-asymmetric evolution in transcribed *Escherichia coli* 1875
1815 sequences. *Mol Biol Evol* 18:1147–1150 1876

1816 90. Frank AC, Lobry JR (1999) Asymmetric substitution patterns: 1877
1817 A review of possible underlying mutational or selective 1878
1818 mechanisms. *Gene* 238:65–77 1879

1819 91. Freeman JM, Plasterer TN, Smith TF, Mohr SC (1998) Patterns 1880
1820 of genome organization in bacteria. *Science* 279:1827 1881

1821 92. Mrázek J, Karlin S (1998) Strand compositional asymmetry in 1882
1822 bacterial and large viral genomes. *Proc Natl Acad Sci USA* 1883
1823 95:3720–3725 1884

93. Rocha EP, Danchin A, Viari A (1999) Universal replication bi- 1885
ases in bacteria. *Mol Microbiol* 32:11–16 1886

94. Tillier ER, Collins RA (2000) The contributions of replication 1887
orientation, gene direction, and signal sequences to base- 1888
composition asymmetries in bacterial genomes. *J Mol Evol* 1889
50:249–257 1890

95. Green P, Ewing B, Miller W, Thomas PJ, Green ED (2003) Trans- 1891
scription-associated mutational asymmetry in mammalian 1892
evolution. *Nat Genet* 33:514–517 1893

96. Touchon M, Nicolay S, Arneodo A, d'Aubenton-Carafa Y, Thermes 1894
C (2003) Transcription-coupled TA and GC strand asym- 1895
metries in the human genome. *FEBS Lett* 555:579–582 1896

97. Touchon M, Arneodo A, d'Aubenton-Carafa Y, Thermes C (2004) 1897
Transcription-coupled and splicing-coupled strand 1898
asymmetries in eukaryotic genomes. *Nucleic Acids Res* 1899
32:4969–4978 1900

98. Brodie of Brodie E-B, Nicolay S, Touchon M, Audit B, d'Aubenton-Carafa Y, Thermes C, Arneodo A (2005) From 1901
DNA sequence analysis to modeling replication in the human 1902
genome. *Phys Rev Lett* 94:248103 **TS5** 1903

99. Nicolay S, Argoul F, Touchon M, d'Aubenton-Carafa Y, Thermes C, Arneodo A (2004) Low frequency rhythms in human 1904
DNA sequences: A key to the organization of gene location 1905
and orientation? *Phys Rev Lett* 93:108101 **TS5** 1906

100. Touchon M, Nicolay S, Audit B, Brodie of Brodie E-B, d'Aubenton-Carafa Y, Arneodo A, Thermes C (2005) Replication- 1907
associated strand asymmetries in mammalian genomes: 1908
Toward detection of replication origins. *Proc Natl Acad Sci 1909
USA* 102:9836–9841 1910

101. Huvet M, Nicolay S, Touchon M, Audit B, d'Aubenton-Carafa Y, Arneodo A, Thermes C (2007) Human gene organization 1911
driven by the coordination of replication and transcription. 1912
Genome Res (to appear) **TS7** 1913

102. Arneodo A, Bacry E, Jaffard S, Muzy J-F (1997) Oscillating sin- 1914
gularities on Cantor sets: A grand-canonical multifractal for- 1915
malism. *J Stat Phys* 87:179–209 1916

103. Arneodo A, Bacry E, Jaffard S, Muzy J-F (1998) Singularity 1917
spectrum of multifractal functions involving oscillating singu- 1918
larities. *J Fourier Anal Appl* 4:159–174 1919

104. Parisi G, Frisch U (1985) Fully developed turbulence and in- 1920
termittency. In: Ghil M, Benzi R, Parisi G (eds) *Turbulence* 1921
and predictability in geophysical fluid dynamics and climate 1922
dynamics. *Proc of Int School*. North-Holland, Amsterdam, 1923
pp 84–88 **TS8** 1924

105. Collet P, Lebowitz J, Porzio A (1987) The dimension spectrum 1925
of some dynamical systems. *J Stat Phys* 47:609–644 1926

106. Grassberger P, Badii R, Politi A (1988) Scaling laws for invariant 1927
measures on hyperbolic and non hyperbolic attractors. *J Stat 1928
Phys* 51:135–178 1929

107. Halsey TC, Jensen MH, Kadanoff LP, Procaccia I, Shraiman BI 1930
(1986) Fractal measures and their singularities: The character- 1931
ization of strange sets. *Phys Rev A* 33:1141–1151 1932

108. Paladin G, Vulpiani A (1987) Anomalous scaling laws in multi- 1933
fractal objects. *Phys Rep* 156:147–225 1934

109. Rand D (1989) The singularity spectrum for hyperbolic Cantor 1935
sets and attractors. *Ergod Th Dyn Sys* 9:527–541 1936

TS7 Please update if possible.

TS8 Please provide volume.

110. Argoul F, Arneodo A, Elezgaray J, Grasseau G (1990) Wavelet analysis of the self-similarity of diffusion-limited aggregates and electrodeposition clusters. *Phys Rev A* 41:5537–5560

111. Farmer JD, Ott E, Yorke JA (1983) The dimension of chaotic attractors. *Physica D* 7:153–180

112. Grassberger P, Procaccia I (1983) Measuring the strangeness of strange attractors. *Physica D* 9:189–208

113. Bohr T, Tél T (1988) The thermodynamics of fractals. In: Hao BL (ed) *Direction in chaos*, vol 2. World Scientific, Singapore, pp 194–237

114. Audit B, Nicolay S, Huvet M, Touchon M, d'Aubenton-Carafa Y, Thermes C, Arneodo A (2007) DNA replication timing data corroborate in silico human replication origin predictions. *Phys Rev Lett* (submitted) **T57**

115. Mandelbrot BB, van Ness JW (1968) Fractional Brownian motions, fractal noises and applications. *SIAM Rev* 10:422–437

116. Arneodo A, Bacry E, Muzy JF (1998) Random cascades on wavelet dyadic trees. *J Math Phys* 39:4142–4164

117. Benzi R, Biferale L, Crisanti A, Paladin G, Vergassola M, Vulpiani A (1993) A random process for the construction of multiaffine fields. *Physica D* 65:352–358

118. Mandelbrot BB (1974) Intermittent turbulence in self-similar cascades: Divergence of high moments and dimension of the carrier. *J Fluid Mech* 62:331–358

119. Arneodo A, Bacry E, Manneville S, Muzy JF (1998) Analysis of random cascades using space-scale correlation functions. *Phys Rev Lett* 80:708–711

120. Castaing B, Dubrulle B (1995) Fully-developed turbulence – A unifying point-of-view. *J Phys II France* 5:895–899

121. Novikov EA (1994) Infinitely divisible distributions in turbulence. *Phys Rev E* 50:3303–3305

122. Gojobori T, Li WH, Graur D (1982) Patterns of nucleotide substitution in pseudogenes and functional genes. *J Mol Evol* 18:360–369

123. Li WH, Wu CI, Luo CC (1984) Nonrandomness of point mutation as reflected in nucleotide substitutions in pseudogenes and its evolutionary implications. *J Mol Evol* 21:58–71

124. Petrov DA, Hartl DL (1999) Patterns of nucleotide substitution in *Drosophila* and mammalian genomes. *Proc Natl Acad Sci USA* 96:1475–1479

125. Zhang Z, Gerstein M (2003) Patterns of nucleotide substitution, insertion and deletion in the human genome inferred from pseudogenes. *Nucleic Acids Res* 31:5338–5348

126. Duret L (2002) Evolution of synonymous codon usage in metazoans. *Curr Opin Genet Dev* 12:640–649

127. Shioiri C, Takahata N (2001) Skew of mononucleotide frequencies, relative abundance of dinucleotides, and DNA strand asymmetry. *J Mol Evol* 53:364–376

128. Svejstrup JQ (2002) Mechanisms of transcription-coupled DNA repair. *Nat Rev Mol Cell Biol* 3:21–29

129. Nicolay S, Brodie of Brodie E-B, Touchon M, Audit B, d'Aubenton-Carafa Y, Thermes C, Arneodo A (2007) Bifractality of human DNA strand-asymmetry profiles results from transcription. *Phys Rev E* 75:032902 **T55**

130. Lee TI, Jenner RG, Boyer LA, Guenther MG, Levine SS, Kumar RM, Chevalier B, Johnstone SE, Cole MF, ichi Isomo K, Koseki H, Fuchikami T, Abe K, Murray HL, Zucker JP, Yuan B, Bell GW, Herbolsheimer E, Hannett NM, Sun K, Odom DT, Otte AP, Volkert TL, Bartel DP, Melton DA, Gifford DK, Jaenisch R, Young RA (2006) Control of developmental regulators by polycomb in human embryonic stem cells. *Cell* 125:301–313

131. Jacob F, Brenner S, Cuzin F (1963) On the regulation of DNA replication in bacteria. *Cold Spring Harb Symp Quant Biol* 28:329–342

132. Bell SP, Dutta A (2002) DNA replication in eukaryotic cells. *Annu Rev Biochem* 71:333–374

133. Anglana M, Apiou F, Bensimon A, Debatisse M (2003) Dynamics of DNA replication in mammalian somatic cells: Nucleotide pool modulates origin choice and interorigin spacing. *Cell* 114:385–394

134. Fisher D, Méchali M (2003) Vertebrate HoxB gene expression requires DNA replication. *EMBO J* 22:3737–3748

135. Gerbi SA, Bielinsky AK (2002) DNA replication and chromatin. *Curr Opin Genet Dev* 12:243–248

136. Hyrien O, Méchali M (1993) Chromosomal replication initiates and terminates at random sequences but at regular intervals in the ribosomal DNA of *Xenopus* early embryos. *EMBO J* 12:4511–4520

137. Schübeler D, Scalzo D, Kooperberg C, van Steensel B, Darrow J, Groudine M (2002) Genome-wide DNA replication profile for *Drosophila melanogaster*: A link between transcription and replication timing. *Nat Genet* 32:438–442

138. Gilbert DM (2001) Making sense of eukaryotic DNA replication origins. *Science* 294:96–100

139. Coverley D, Laskey RA (1994) Regulation of eukaryotic DNA replication. *Annu Rev Biochem* 63:745–776

140. Sasaki T, Sawado T, Yamaguchi M, Shinomiya T (1999) Specification of regions of DNA replication initiation during embryogenesis in the 65-kilobase DNApolalpha-dE2F locus of *Drosophila melanogaster*. *Mol Cell Biol* 19:547–555

141. Bogen JA, Natale DA, DePamphilis ML (2000) Initiation of eukaryotic DNA replication: Conservative or liberal? *J Cell Physiol* 184:139–150

142. Gilbert DM (2004) In search of the holy replicator. *Nat Rev Mol Cell Biol* 5:848–855

143. Demeret C, Vassetzky Y, Méchali M (2001) Chromatin remodeling and DNA replication: From nucleosomes to loop domains. *Oncogene* 20:3086–3093

144. McNairn AJ, Gilbert DM (2003) Epigenomic replication: linking epigenetics to DNA replication. *Bioessays* 25:647–656

145. Méchali M (2001) DNA replication origins: From sequence specificity to epigenetics. *Nat Rev Genet* 2:640–645

146. Arneodo A, d'Aubenton-Carafa Y, Audit B, Brodie of Brodie E-B, Nicolay S, St-Jean P, Thermes C, Touchon M, Vaillant C (2007) DNA in chromatin: From genome-wide sequence analysis to the modeling of replication in mammals. *Adv Chem Phys* 135:203–252

147. Bulmer M (1991) Strand symmetry of mutation rates in the beta-globin region. *J Mol Evol* 33:305–310

148. Francino MP, Ochman H (2000) Strand symmetry around the beta-globin origin of replication in primates. *Mol Biol Evol* 17:416–422

149. Gierlik A, Kowalcuk M, Mackiewicz P, Dudek MR, Cebrat S (2000) Is there replication-associated mutational pressure in the *Saccharomyces cerevisiae* genome? *J Theor Biol* 202: 305–314

150. Berezney R, Dubey DD, Huberman JA (2000) Heterogeneity of eukaryotic replicons, replicon clusters, and replication foci. *Chromosoma* 108:471–484

151. Vassilev LT, Burhans WC, DePamphilis ML (1990) Mapping an origin of DNA replication at a single-copy locus in *ex-*

2001 ponentially proliferating mammalian cells. *Mol Cell Biol* 10: 4685–4689

2002

2003 152. Codlin S, Dalgaard JZ (2003) Complex mechanism of site-specific DNA replication termination in fission yeast. *EMBO J* 22:3431–3440

2004

2005 153. Little RD, Platt TH, Schildkraut CL (1993) Initiation and termination of DNA replication in human rRNA genes. *Mol Cell Biol* 13:6600–6613

2006

2007

2008 154. Santamaría D, Viguera E, Martinez-Robles ML, Hyrien O, Hernandez P, Krimer DB, Schwartzman JB (2000) Bi-directional replication and random termination. *Nucleic Acids Res* 28:2099–2107

2009

2010

2011 155. White EJ, Emanuelsson O, Scalzo D, Royce T, Kosak S, Oakeley EJ, Weissman S, Gerstein M, Groudine M, Snyder M, Schübeler D (2004) DNA replication-timing analysis of human chromosome 22 at high resolution and different developmental states. *Proc Natl Acad Sci USA* 101:17771–17776

2012

2013

2014 156. Woodfine K, Beare DM, Ichimura K, Debernardi S, Mungall AJ, Fiegler H, Collins VP, Carter NP, Dunham I (2005) Replication timing of human chromosome 6. *Cell Cycle* 4:172–176

2015

2016

2017 157. Raghuraman MK, Winzeler EA, Collingwood D, Hunt S, Wodicka L, Conway A, Lockhart DJ, Davis RW, Brewer BJ, Fangman WL (2001) Replication dynamics of the yeast genome. *Science* 294:115–121

2018

2019

2020 158. Watanabe Y, Fujiyama A, Ichiba Y, Hattori M, Yada T, Sakaki Y, Ikemura T (2002) Chromosome-wide assessment of replication timing for human chromosomes 11q and 21q: Disease-related genes in timing-switch regions. *Hum Mol Genet* 11:13–21

2021

2022

2023 159. Costantini M, Clay O, Federico C, Saccone S, Auletta F, Bernardi G (2007) Human chromosomal bands: Nested structure, high-definition map and molecular basis. *Chromosoma* 116:29–40

2024

2025

2026 160. Schmegner C, Hameister H, Vogel W, Assum G (2007) Isochores and replication time zones: A perfect match. *Cytogenet Genome Res* 116:167–172

2027

2028

2029 161. Chakalova L, Debrand E, Mitchell JA, Osborne CS, Fraser P (2005) Replication and transcription: shaping the landscape of the genome. *Nat Rev Genet* 6:669–677

2030

2031

2032 162. Gilbert N, Boyle S, Fiegler H, Woodfine K, Carter NP, Bickmore WA (2004) Chromatin architecture of the human genome: Gene-rich domains are enriched in open chromatin fibers. *Cell* 118:555–566

2033

2034

2035 163. Hurst LD, Pál C, Lercher MJ (2004) The evolutionary dynamics of eukaryotic gene order. *Nat Rev Genet* 5:299–310

2036

2037

2038 164. Sproul D, Gilbert N, Bickmore WA (2005) The role of chromatin structure in regulating the expression of clustered genes. *Nat Rev Genet* 6:775–781

2039

2040

2041 165. MacAlpine DM, Rodriguez HK, Bell SP (2004) Coordination of replication and transcription along a *Drosophila* chromosome. *Genes Dev* 18:3094–3105

2042

2043

2044 166. Danis E, Brodolin K, Menut S, Maiorano D, Girard-Reydet C, Méchali M (2004) Specification of a DNA replication origin by a transcription complex. *Nat Cell Biol* 6:721–730

2045

2046

2047 167. DePamphilis ML (2005) Cell cycle dependent regulation of the origin recognition complex. *Cell Cycle* 4:70–79

2048

2049

2050 168. Ghosh M, Liu G, Randall G, Bevington J, Leffak M (2004) Transcription factor binding and induced transcription alter chromosomal c-myc replicator activity. *Mol Cell Biol* 24: 10193–10207

2051

2052

2053

2054

2055

2056

2057

2058

2059

2060

169. Lin CM, Fu H, Martinovsky M, Bouhassira E, Aladjem MI (2003) Dynamic alterations of replication timing in mammalian cells. *Curr Biol* 13:1019–1028

2061

2062

2063

170. Jeon Y, Bekiranov S, Karnani N, Kapranov P, Ghosh S, MacAlpine D, Lee C, Hwang DS, Gingeras TR, Dutta A (2005) Temporal profile of replication of human chromosomes. *Proc Natl Acad Sci USA* 102:6419–6424

2064

2065

2066

2067

171. Deshpande AM, Newlon CS (1996) DNA replication fork pause sites dependent on transcription. *Science* 272:1030–1033

2068

172. Takeuchi Y, Horiuchi T, Kobayashi T (2003) Transcription-dependent recombination and the role of fork collision in yeast rDNA. *Genes Dev* 17:1497–1506

2069

173. Rocha EPC, Danchin A (2003) Essentiality, not expressiveness, drives gene-strand bias in bacteria. *Nat Genet* 34:377–378

2070

174. Herrick J, Stanislawski P, Hyrien O, Bensimon A (2000) Replication fork density increases during DNA synthesis in *X. laevis* egg extracts. *J Mol Biol* 300:1133–1142

2071

175. Zlatanova J, Leuba SH (2003) Chromatin fibers, one-at-a-time. *J Mol Biol* 331:1–19

2072

176. Tassius C, Moskalenko C, Minard P, Desmadril M, Elezgaray J, Argoul F (2004) Probing the dynamics of a confined enzyme by surface plasmon resonance. *Physica A* 342:402–409

2073

177. Müller WG, Rieder D, Kreth G, Cremer C, Trajanoski Z, McNally JG (2004) Generic features of tertiary chromatin structure as detected in natural chromosomes. *Mol Cell Biol* 24: 9359–9370

2074

2075

2076

2077

2078

2079

2080

2081

2082

2083

2084

2085

2086

Books and Reviews

Fractals

Aharony A, Feder J (eds) (1989) *Fractals in Physics, Essays in Honour of BB Mandelbrot*. *Physica D* 38. North-Holland, Amsterdam

Avnir D (ed) (1988) *The fractal approach to heterogeneous chemistry: surfaces, colloids, polymers*. Wiley, New-York

Barabàsi AL, Stanley HE (1995) *Fractals concepts in surface growth*. Cambridge University Press, Cambridge

Ben Avraham D, Havlin S (2000) *Diffusion and reactions in fractals and disordered systems*. Cambridge University Press, Cambridge

Bouchaud J-P, Potters M (1997) *Théorie des risques financiers*. Cambridge University Press, Cambridge

Bunde A, Havlin S (eds) (1991) *Fractals and disordered systems*. Springer, Berlin

Bunde A, Havlin S (eds) (1994) *Fractals in science*. Springer, Berlin

Bunde A, Kropp J, Schellnhuber HJ (eds) (2002) *The science of disasters: Climate disruptions, heart attacks and market crashes*. Springer, Berlin

Family F, Meakin P, Sapoval B, Wood R (eds) (1995) *Fractal aspects of materials*. Material Research Society Symposium Proceedings, vol 367. MRS, Pittsburg

Family F, Vicsek T (1991) *Dynamics of fractal surfaces*. World Scientific, Singapore

Feder J (1988) *Fractals*. Pergamon, New-York

Frisch U (1995) *Turbulence*. Cambridge University Press, Cambridge

Mandelbrot BB (1982) *The Fractal Geometry of Nature*. Freeman, San Francisco

Mantegna RN, Stanley HE (2000) *An introduction to econophysics*. Cambridge University Press, Cambridge

Meakin P (1998) *Fractals, scaling and growth far from equilibrium*. Cambridge University Press, Cambridge

2120 Peitgen HO, Jürgens H, Saupe D (1992) *Chaos and fractals: New frontiers of science*. Springer, New York
 2121 Peitgen HO, Saupe D (eds) (1987) *The science of fractal images*. Springer, New-York
 2122 Pietronero L, Tosatti E (eds) (1986) *Fractals in physics*. North-Holland, Amsterdam
 2123 Stanley HE, Ostrowski N (eds) (1986) *On growth and form: Fractal and non-fractal patterns in physics*. Martinus Nijhof, Dordrecht
 2124 Stanley HE, Ostrowski N (eds) (1988) *Random fluctuations and pattern growth*. Kluwer, Dordrecht
 2125 Vicsek T (1989) *Fractal growth phenomena*. World Scientific, Singapore
 2126 Vicsek T, Schlesinger M, Matsuchita M (eds) (1994) *Fractals in natural science*. World Scientific, Singapore
 2127 West BJ (1990) *Fractal physiology and chaos in medicine*. World Scientific, Singapore
 2128 West BJ, Deering W (1994) *Fractal physiology for physicists: Levy statistics*. *Phys Rep* 246:1–100
 2129 Wilkinson GG, Kanellopoulos J, Megier J (eds) (1995) *Fractals in geo-science and remote sensing, image understanding research series*, vol 1. ECSC-EC-EAAC, Brussels
 2130
 2131
 2132
 2133
 2134
 2135
 2136
 2137
 2138
 2139
 2140
 2141
 2142
 2143
 2144
 2145
 2146
 2147
 2148
 2149
 2150
 2151
 2152
 2153
 2154
 2155
 2156
 2157
 2158
 2159
 2160
 2161
 2162
 2163
 2164
 2165
 2166
 2167
 2168
 2169
 2170
 2171
 2172
 2173
 2174
 2175
 2176
 2177
 2178

Calladine CR, Drew HR (1999) *Understanding DNA*. Academic Press, San Diego
 2179
 2180
 Graur D, Li WH (1999) *Fundamentals of molecular evolution*. Sinauer Associates, Sunderland
 2181
 2182
 Hartl DL, Jones EW (2001) *Genetics: Analysis of genes and genomes*. Jones and Bartlett, Sudbury
 2183
 2184
 Kolchanov NA, Lim HA (1994) *Computer analysis of genetic macromolecules: Structure, function and evolution*. World Scientific, Singapore
 2185
 2186
 2187
 Kornberg A, Baker TA (1992) *DNA Replication*. WH Freeman, New-York
 2188
 2189
 Lewin B (1994) *Genes V*. Oxford University Press, Oxford
 2190
 Sudbery P (1998) *Human molecular genetics*. Addison Wesley, Singapore
 2191
 2192
 Van Holde KE (1988) *Chromatin*. Springer, New-York
 2193
 Watson JD, Gilman M, Witkowski J, Zoller M (1992) *Recombinant DNA*. Freeman, New-York
 2194
 2195
 Wolfe AP (1998) *Chromatin structure and function*, 3rd edn. Academic Press, London
 2196
 2197

Wavelets

Abry P (1997) *Ondelettes et turbulences*. Diderot Éditeur, Art et Sciences, Paris
 Arneodo A, Argoul F, Bacry E, Elezgaray J, Muzy J-F (1995) *Ondelettes, multifractales et turbulences: de l'ADN aux croissances cristallines*. Diderot Éditeur, Art et Sciences, Paris
 Chui CK (1992) *An introduction to wavelets*. Academic Press, Boston
 Combes J-M, Grossmann A, Tchamitchian P (eds) (1989) *Wavelets*. Springer, Berlin
 Daubechies I (1992) *Ten lectures on wavelets*. SIAM, Philadelphia
 Erlebacher G, Hussaini MY, Jameson LM (eds) (1996) *Wavelets: Theory and applications*. Oxford University Press, Oxford
 Farge M, Hunt JCR, Vassilicos JC (eds) (1993) *Wavelets, fractals and Fourier*. Clarendon Press, Oxford
 Flandrin P (1993) *Temps-Fréquence*. Hermès, Paris
 Holschneider M (1996) *Wavelets: An analysis tool*. Oxford University Press, Oxford
 Jaffard S, Meyer Y, Ryan RD (eds) (2001) *Wavelets: Tools for science and technology*. SIAM, Philadelphia
 Lemarie PG (ed) (1990) *Les ondelettes en 1989*. Springer, Berlin
 Mallat S (1998) *A wavelet tour in signal processing*. Academic Press, New-York
 Meyer Y (1990) *Ondelettes*. Herman, Paris
 Meyer Y (ed) (1992) *Wavelets and applications*. Springer, Berlin
 Meyer Y, Roques S (eds) (1993) *Progress in wavelets analysis and applications*. Éditions Frontières, Gif-sur-Yvette
 Ruskai MB, Beylkin G, Coifman R, Daubechies I, Mallat S, Meyer Y, Raphael L (eds) (1992) *Wavelets and their applications*. Jones and Barlett, Boston
 Silverman BW, Vassilicos JC (eds) (2000) *Wavelets: The key to intermittent information?* Oxford University Press, Oxford
 Torresani B (1998) *Analyse continue par ondelettes*. Éditions de Physique, Les Ulis

DNA and Chromatin

Alberts B, Watson J (1994) *Molecular biology of the cell*, 3rd edn. Garland Publishing, New-York